Cell

# Structural Rearrangement of Ebola Virus VP40 Begets Multiple Functions in the Virus Life Cycle

Zachary A. Bornholdt,[1] Takeshi Noda,[4] Dafna M. Abelson,[1] Peter Halfmann,[6] Malcolm R. Wood,[2] Yoshihiro Kawaoka,[4,5,6,7] and Erica Ollmann Saphire[1,3,*]

[1]Department of Immunology and Microbial Science
[2]Core Microscopy Facility
[3]The Skaggs Institute for Chemical Biology
The Scripps Research Institute, La Jolla, CA 92037, USA
[4]Division of Virology, Department of Microbiology and Immunology
[5]International Research Center for Infectious Diseases
Institute of Medical Science, University of Tokyo, Tokyo 108-8639, Japan
[6]Department of Pathobiological Sciences, School of Veterinary Medicine, University of Wisconsin-Madison, Madison, WI 53706, USA
[7]Infection-Induced Host Responses Project, Exploratory Research for Advanced Technology, Saitama 332-0012, Japan
*Correspondence: erica@scripps.edu
http://dx.doi.org/10.1016/j.cell.2013.07.015

## SUMMARY

Proteins, particularly viral proteins, can be multifunctional, but the mechanisms behind multifunctionality are not fully understood. Here, we illustrate through multiple crystal structures, biochemistry, and cellular microscopy that VP40 rearranges into different structures, each with a distinct function required for the ebolavirus life cycle. A butterfly-shaped VP40 dimer traffics to the cellular membrane. Once there, electrostatic interactions trigger rearrangement of the polypeptide into a linear hexamer. These hexamers construct a multilayered, filamentous matrix structure that is critical for budding and resembles tomograms of authentic virions. A third structure of VP40, formed by a different rearrangement, is not involved in virus assembly but instead uniquely binds RNA to regulate viral transcription inside infected cells. These results provide a functional model for ebolavirus matrix assembly and the other roles of VP40 in the virus life cycle and demonstrate how a single wild-type, unmodified polypeptide can assemble into different structures for different functions.

## INTRODUCTION

Ebolaviruses cause severe hemorrhagic fever with up to 90% lethality and are considered potential biological weapons (Bwaka et al., 1999; Kuhn, 2008). There are five antigenically distinct ebolaviruses, each named after the outbreak location in which they were first discovered. Of these, the two most common are Ebola virus and Sudan virus (Kuhn et al., 2011; Adams et al., 2012). Ebolaviruses encode just seven genes and are distinguished by their pleomorphic filamentous morphology (Kuhn, 2008). Ebolaviruses assemble and bud from the cell membrane in a process driven by the viral matrix protein VP40 (Harty et al., 2000; Panchal et al., 2003). VP40 alone is sufficient to assemble and bud filamentous virus-like particles (VLPs) from cells (Geisbert and Jahrling, 1995; Johnson et al., 2006; Noda et al., 2002).

The first crystal structure of VP40 suggested that this protein is monomeric (Dessen et al., 2000a, 2000b). The structure revealed that VP40 contains distinct N- and C-terminal domains (NTDs and CTDs, respectively), both essential for trafficking to and interaction with the membrane (Harty, 2009; Jasenosky et al., 2001). The limited number of contacts observed between the NTD and CTD suggests that they are tenuously connected and could separate to assemble a different structure (Dessen et al., 2000b; Gomis-Rüth et al., 2003). Indeed, when VP40 is incubated with urea and RNA or liposomes, conformational changes occur, and the NTD then drives the assembly of RNA-binding ring structures (Harty, 2009). A crystal structure of a VP40 ring was solved by expressing the VP40 NTD alone. In the structure, eight VP40 NTDs assemble into a ring with each NTD bound to an RNA trinucleotide (Gomis-Rüth et al., 2003).

Currently, the VP40 ring and the interfaces by which it assembles provide the only known structural model of how VP40 might assemble the ebolavirus matrix. However, these rings are observed only in infected cells, not in mature purified ebolaviruses (Gomis-Rüth et al., 2003), suggesting the ring structure is not involved in matrix assembly. Instead, the RNA-binding VP40 rings likely play a critical, but currently undefined role inside the infected cell (Gomis-Rüth et al., 2003; Hoenen et al., 2010a).

Despite the wealth of structural and biochemical data, no cohesive model exists for how the ebolavirus matrix is assembled. It is currently unclear which structure of VP40 migrates to the cell membrane and how that structure is triggered to further oligomerize into the viral matrix. Although RNA binding by VP40 is critical to the viral life cycle (Hoenen et al., 2005),

the exact role of the VP40 RNA-binding ring has remained elusive. In addition and perhaps most significantly, the structural arrangement of VP40 within the ebolavirus matrix remains unknown. Here, we set out to provide a structurally and biologically supported model of VP40-driven matrix assembly and elucidate the different roles played by VP40 in the ebolavirus life cycle.

We first purified VP40 and determined that it is a dimer in solution, not a monomer. We then determined multiple crystal structures of dimeric VP40, from Ebola virus and Sudan virus, revealing a conserved dimeric interface. Targeted mutagenesis of the dimer interface abolishes trafficking of VP40 to the cell membrane and budding of VLPs, suggesting that the VP40 dimer is a critical precursor of the viral matrix. We next analyzed a conserved CTD-to-CTD interface by which VP40 dimers are linked together in crystals. Structure-based mutagenesis of the CTD-to-CTD interface abolishes assembly and budding of virus-like particles, but not trafficking to or interactions with the membrane. Thus, assembly of VP40 dimers via CTD interactions likely represents a critical step in matrix assembly.

We next turned our attention to understanding how the VP40 dimer interacts with the membrane and conformational changes believed to occur at the membrane and be important to matrix assembly. Previous work has demonstrated that electrostatic interactions between the VP40 CTD and the membrane are likely important to matrix assembly (Adu-Gyamfi et al., 2012; Ruigrok et al., 2000; Scianimanico et al., 2000). Through targeted mutagenesis, we identified a conserved basic patch in the CTD that mediates both membrane interaction and subsequent matrix assembly events. An electrostatic mimic of the membrane was found to trigger conformational rearrangement of VP40 dimers into a linear hexameric assembly. In the crystal structure of this assembly, VP40 hexamers also connect into continuous filaments via the conserved CTD interactions. We propose that the VP40 hexamer structure represents a building block of the flexible, filamentous ebolavirus matrix. Our hexameric VP40 structure suggests that VP40 assembles into a multilayered matrix along the membrane, which is consistent with recent electron tomographic analysis of filoviruses in scale, dimension, and layered construction (Beniac et al., 2012; Bharat et al., 2011).

We also determined that the VP40 RNA-binding ring structure, although derived from the VP40 dimer, is not involved in or required for matrix assembly and budding. Instead, we show that the VP40 ring plays a distinct and critical role in regulation of viral transcription inside infected cells and that this function is dependent on its unique RNA-binding capability.

Taken together, our results illustrate that the highly plastic VP40 polypeptide is able to rearrange itself into distinct structural assemblies. Each of these distinct structures is assembled by the unmodified wild-type polypeptide, and each structure is required for a separate and essential function in the virus life cycle: a dimeric precursor critical for cellular trafficking, a hexameric structural component for the viral matrix assembly, and a nonstructural RNA-binding ring structure essential for regulating viral transcription. Thus, the physical plasticity inherent in VP40 demonstrates how a structural rearrangement can expand the functional repertoire of a single viral gene.

## RESULTS

### Ebolavirus VP40 Is a Dimer in Solution

Three constructs of VP40 were expressed without fusion partners, purified, and subjected to size-exclusion chromatography and multiangle light scattering (SEC-MALS). These included wild-type full-length Ebola virus VP40 (WT-VP40E) and Ebola and Sudan virus VP40 with a deletion of 43 residues from the disordered N terminus in order to improve crystal diffraction (VP40EΔN and VP40SΔN, respectively) (Figure 1A). All three VP40 proteins consistently elute from size-exclusion columns as dimers and maintain molecular weights consistent with a dimer via SEC-MALS analysis, a more sensitive method for accurate molecular weight determination than size-exclusion chromatography alone (Wyatt, 1998) (Figure S1 available online). This result is in contrast to previous work in which VP40 (also containing an N-terminal deletion of 30 residues) was characterized as a monomer ($VP40E_M$) (Dessen et al., 2000a, 2000b).

### Crystal Structures of Sudan and Ebola Virus VP40 Identify the Dimeric Interface of Ebolavirus VP40

The VP40SΔN protein crystallizes in the space group C2 with one protomer in the crystallographic asymmetric unit (ASU) and diffracts to 1.8 Å resolution. The VP40EΔN protein crystallizes in the space group $P6_2$ with four protomers in the ASU and diffracts to 3.1 Å resolution. In all of these crystal structures, the overall protein architecture remains conserved with the previously determined $VP40E_M$ (Dessen et al., 2000b): the NTD contains a β sandwich decorated by four small α helices, whereas the CTD contains some disordered loop structure that links two small β sheets and two α helices. Here, we detail the structure of the dimeric interface conserved in the crystal structures (Figure 1).

There is one protein-protein interface that is completely conserved throughout crystals of VP40EΔN and VP40SΔN, suggesting that it assembles the in-solution dimer. The interface appears between the NTDs of two VP40 protomers and buries 1,500–1,700 $Å^2$ of molecular surface, depending on the viral species of the VP40 (Figures 1B). Although not previously described, this dimeric interface is also conserved between symmetry-related protomers in the crystal packing of $VP40E_M$ (Dessen et al., 2000b). Overall, the dimers are structurally conserved with a root-mean-square deviation (rmsd) of 0.45 to 0.88 Å (Figure S2).

The VP40 dimeric interface involves residues 52–65 and 108–117, which encompass two α helices (residues 61–65 and 108–116). Interactions within the VP40 dimeric interface have limited hydrogen bonding and are primarily hydrophobic in nature. The hydrophobic network in the dimer interface involves residues A55, H61, F108, T112, A113, M116, and L117, of which L117 appears to be of central importance. L117 extends into a hydrophobic pocket formed by residues H61, A55, M116, and F108 in the opposing subunit and appears to lock the VP40 protomers together into a dimer (Figure 1C).

### The Dimer Interface Is Essential for Matrix Assembly and Viral Budding

Mutagenesis was performed to verify the biological relevance of the conserved VP40 dimeric interface. Two mutations were

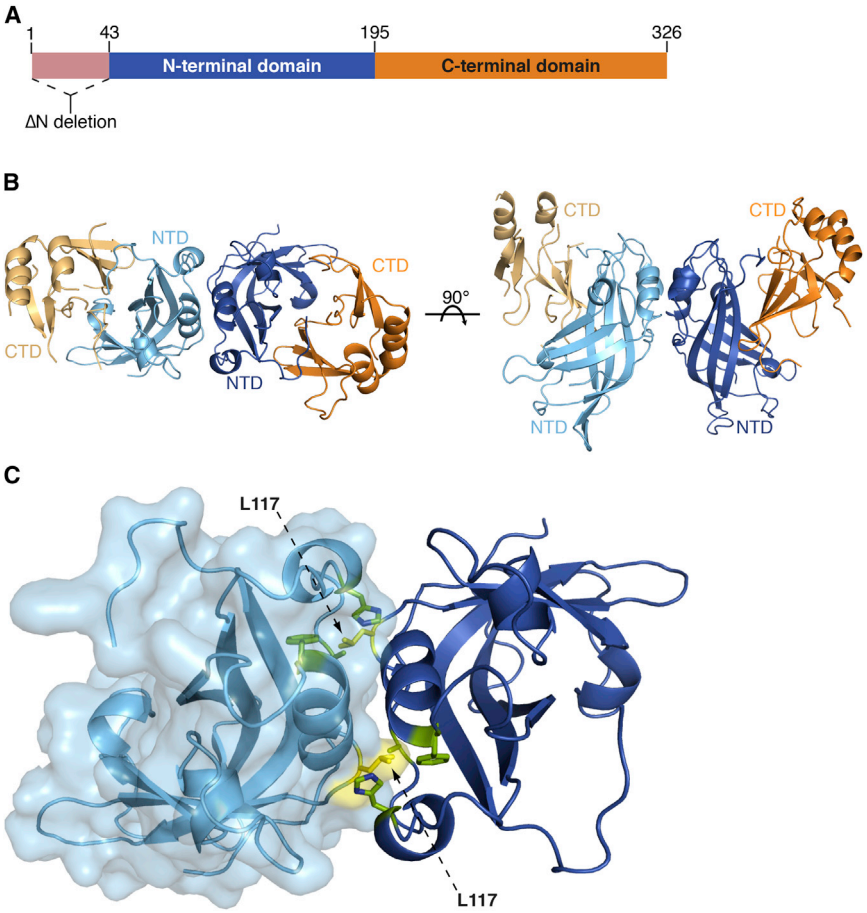


**Figure 1. The Dimeric Structure of VP40**

(A) A schematic of VP40 showing the location of the N-terminal 43 residue deletion in VP40SΔN and VP40EΔN and the NTD (blue) and CTD (orange).

(B) The VP40EΔN dimeric crystal structure is displayed with the NTDs from each protomer colored light or dark blue and the CTDs colored light or dark orange.

(C) The VP40EΔN dimeric interface displaying residues A55, H61, F108, A113, and M116 (green) and L117 (yellow). The surface representation on the light blue protomer illustrates how L117 reaches into the opposing protomer.

See also Figures S1 and S2.

made, L117R and T112R (VP40EΔN-L117R and VP40EΔN-T112R), as modeling suggested that the larger arginine side chain in these positions would disrupt the VP40 dimeric interface (Figure 2A). Indeed, purified VP40EΔN-L117R and VP40EΔN-T112R are primarily monomeric but also assemble some RNA-binding ring structures (Figure S1). Thus, the L117R and T112R mutations have not disrupted the tertiary structure of the VP40 NTD, as a properly folded NTD is essential for ring assembly (Gomis-Rüth et al., 2003).

Western blot analysis of cells transfected with WT-VP40E or the mutants VP40E-L117R or VP40E-T112R showed that, whereas WT-VP40E is successfully released from cells, both mutants are retained within the cell (Figure 2B). Indeed, immunofluorescence analysis (IFA) illustrated that WT-VP40E efficiently buds virus-like particles (VLPs), whereas both VP40E-L117R and VP40E-T112R mutants fail to migrate to the membrane or bud VLPs (Figure 2C). The IFA also indicated that VP40E-T112R has a propensity to form perinuclear inclusions reminiscent of previously observed globular structures formed by VP40 oligomeric rings (Panchal et al., 2003). Transmission electron microscopy (TEM) further showed that, whereas WT-VP40 assembles into filamentous VLPs and buds from the cell membrane, both VP40E-L117R and VP40E-T112R fail to bud and display no signs of assembly at the cell surface (Figure 2D). Thus, the L117R and T112R point mutations disrupt VP40 dimer formation, cellular trafficking, matrix assembly, and budding of ebolavirus-like particles but do not appear to impede the formation of VP40 ring oligomers (Figures 2D and S1).

## VP40 Dimers Further Assemble End-to-End into Filaments that Are Essential for Matrix Assembly and Budding

In all crystal structures of VP40 containing its C-terminal domain, the VP40 dimers further assemble end-to-end into filaments through homologous interactions between their C-terminal domains (Figure 3A and S3). This primarily hydrophobic CTD-to-CTD interface involves residues L203, I237, M241, M305, and I307 and has a smooth topology along the buried surface. The lack of interdigitation along this hydrophobic interface potentially allows for torsional motion between the CTDs. Indeed, potential motion about this interface can be observed in the $P6_2$ crystal packing of VP40EΔN, in which every other dimer is rotated by ~90° along this CTD-to-CTD interface (Figure S3).

Mutagenesis was performed to determine whether the CTD-to-CTD interface was relevant to ebolavirus matrix assembly and formation of filamentous VLPs. Residue M241 is buried in the CTD-to-CTD interface but is not integral to the fold of the CTD. Modeling suggested that replacement of M241 with arginine would impair formation of the CTD-to-CTD interface but would not disrupt VP40 dimerization (Figure 3A). Indeed, purified VP40EΔN-M241R remains primarily dimeric in solution (Figure S1), yet transfected VP40E-M241R does not assemble or bud filamentous VLPs (Figure 3B). The neighboring residue T242, unlike M241, is solvent exposed and does not contribute to the CTD-to-CTD interface. Hence, a control mutant, VP40E-T242R, was also generated to ensure that merely placing an arginine residue in this region of the CTD does not inhibit the function of VP40. As anticipated, VP40E-T242R successfully assembles and buds VLPs at wild-type levels (Figure 3B).

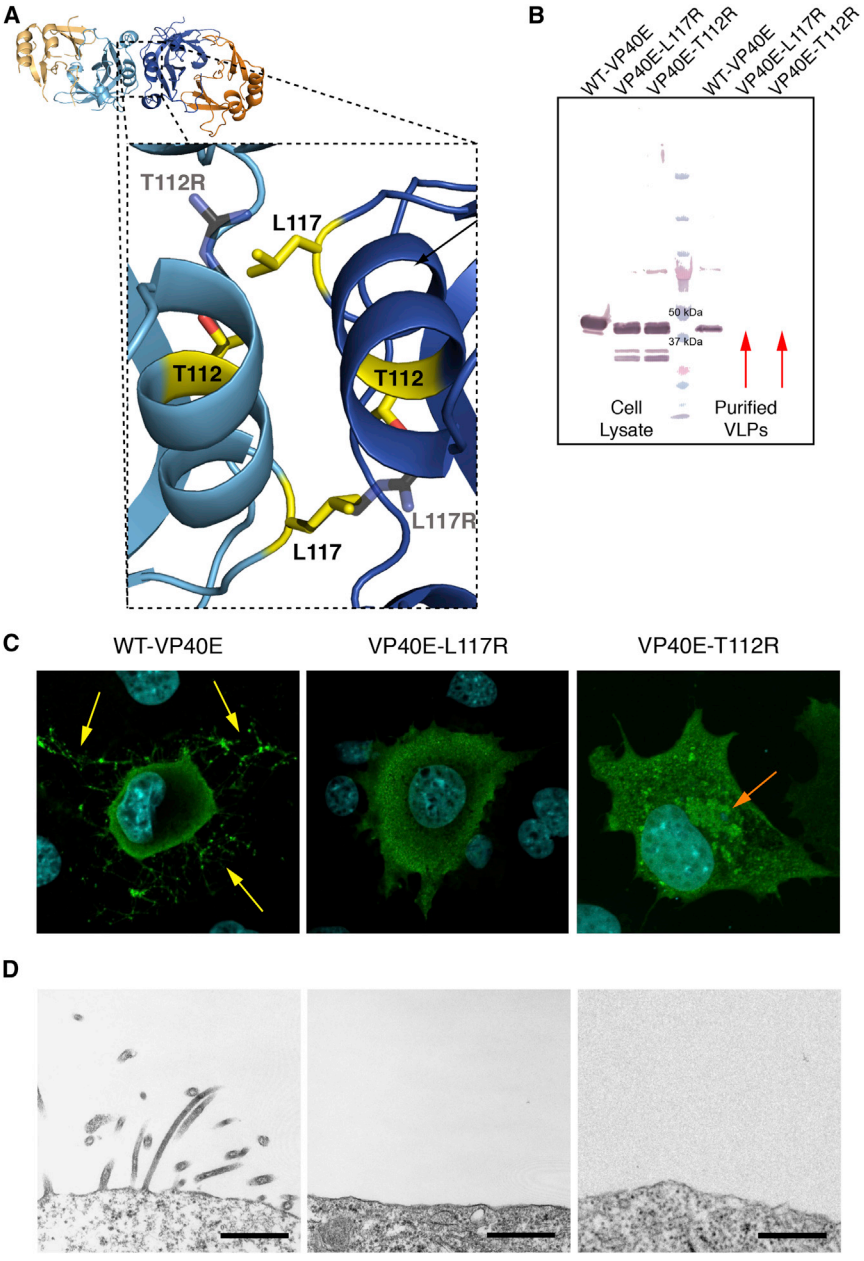


**Figure 2. Analysis of the VP40 Dimeric Interface**

(A) A dashed box displays a close-up view of the dimeric interface, centered on residues T112 and L117 (yellow). The point mutations T112R and L117R have been modeled onto the structure (black).

(B) Western blot of cell lysates and purified VLPs from transfected cells. VP40E-L117R and VP40E-T112R do not bud VLPs from transfected cells (red arrows).

(C) IFA experiments show that WT-VP40E localizes to the cell membrane and buds VLPs (yellow arrows), whereas both VP40E-L117R and VP40E-T112R fail to localize to the membrane or assemble and bud VLPs. VP40E-T112R also forms perinuclear structures (orange arrow).

(D) EM micrographs display active VLP assembly and budding from cells transfected with WT-VP40E, whereas EM micrographs of cells transfected with either VP40E-L117R or VP40E-T112R display no assembly or VLP budding activity. Scale bars, 500 nm.

Interestingly, cells transfected with VP40E-M241R exhibit an exaggerated membrane-ruffling morphology, indicating that VP40E-M241R migrates to and interacts with the cell membrane but still fails to properly assemble the matrix and bud VLPs. This suggests that VP40E-M241R may assemble some intermediate or defective matrix structure along the membrane (Figures 3C and 3D). In order to determine how VP40E-M241R might be assembling, we determined a crystal structure of the mutant. Crystals of VP40EΔN-M241R belong to the space group $P4_12_12$ and diffract to 4.15 Å. The VP40EΔN-M241R structure indicates the VP40 dimer is intact, but interactions along the CTD-to-CTD interface are limited by the M241R mutation. Within the crystal packing, VP40EΔN-M241R fails to assemble any filaments and only interacts with one neighboring dimer via a minimal and twisted CTD-to-CTD interface, with L203 and I307 at the center rather than M241 (Figure S3). This may explain why VP40E-M241R ruffles the cell membrane but fails to bud VLPs, as the M241R mutation allows for a limited assembly of dimers to initiate membrane curvature but fails to complete assembly of the matrix to bud VLPs.

## A Second Point Mutation in the VP40 CTD-to-CTD Interface Automatically Triggers Oligomeric Ring Formation and RNA Binding

Residue I307, similar to M241, is also buried in the CTD-to-CTD interface and was mutated to arginine in order to further investigate the physiological relevance of that interface (Figure 3A). Curiously, the purified VP40EΔN-I307R mutant displays a unique phenotype, in that it does not yield the expected dimers but instead exclusively forms RNA binding oligomeric rings ($A_{260/280} > 1.0$) (Figures S1 and S4).

Western blots of cells transfected with VP40E-I307R indicated that this mutation blocks assembly and budding of VLPs into the supernatant (Figure 3B). Further, IFA showed that, in these cells, VP40E-I307R does not migrate to the cellular membrane but instead assembles into large globular structures around the nucleus (Figure 3C). These perinuclear assemblies are similar to those formed by VP40E-T112R (Figure 2C) and other ring-forming VP40 mutants (Panchal et al., 2003). A control mutant analogous to VP40E-T242R was also generated: VP40E-Q309R.

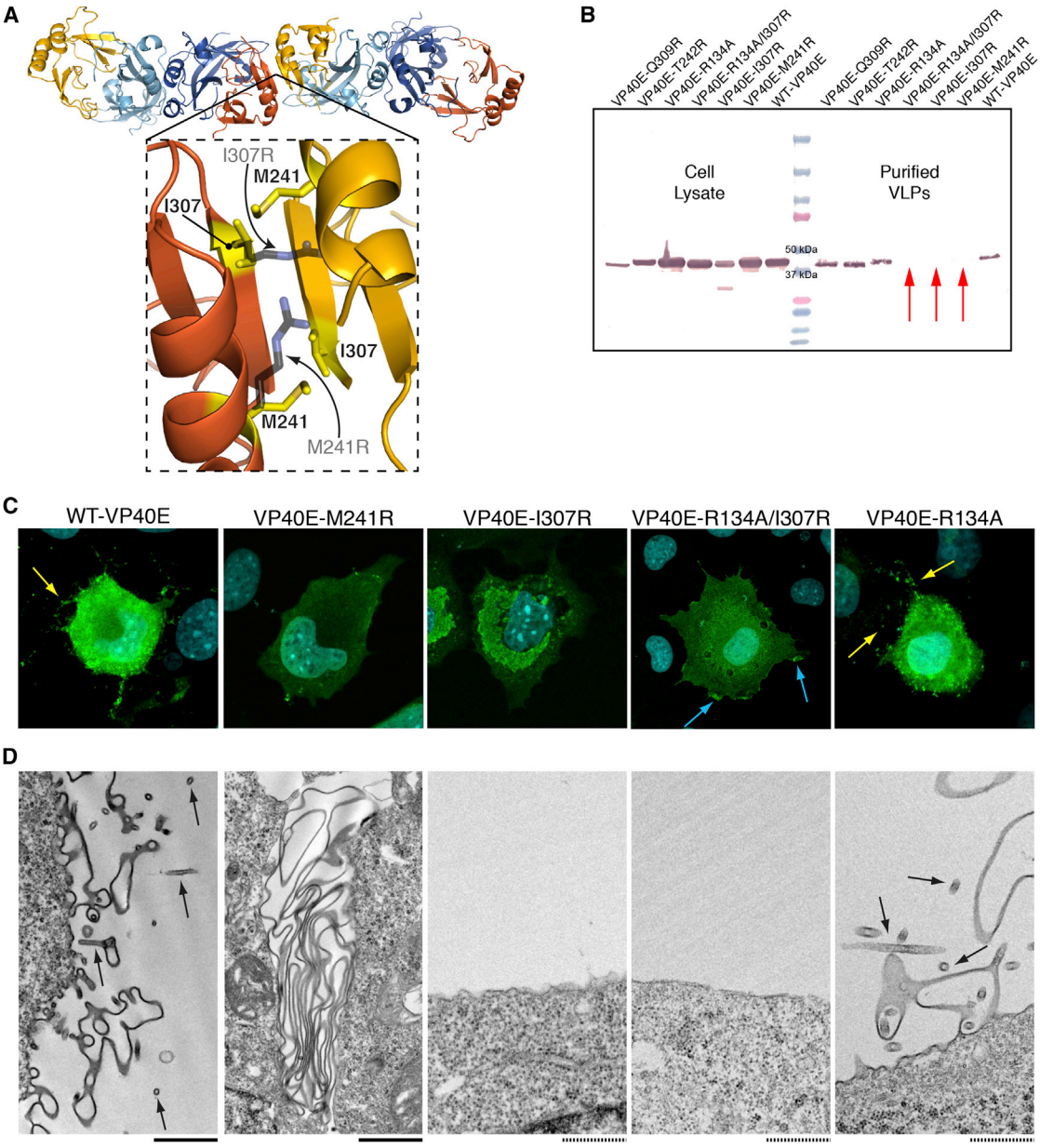


**Figure 3. Analysis of the VP40 CTD-to-CTD Interface**

(A) The CTD-to-CTD interface between VP40 dimers is shown with the NTDs from each protomer colored light or dark blue and the CTDs colored light or dark orange. Below: a view of the CTD-to-CTD interface around residues M241 and I307 (yellow), with the disruptive mutations M241R and I307R (black) modeled onto the orange CTD.

(B) Western blot of cell lysates and purified VLPs from transfected cells. Disruptive CTD-to-CTD interface point mutants, VP40E-M241R, VP40E-I307R, and VP40E-R134A/I307R, fail to bud VLPs (red arrows). The CTD control mutants, VP40E-T242R and VP40E-Q309R, successfully assemble and bud VLPs.

(C) IFA of transfected cells shows that dimeric WT-VP40E and VP40E-R134A migrate to the cell membrane and bud VLPs (yellow arrows). In contrast, VP40E-M241R and VP40E-R134A/I307R, bearing point mutations to the CTD-to-CTD interface, similarly migrate to the cell membrane but do not bud VLPs. Patches of VP40E-R134A/I307R accumulated at the membrane are indicated by blue arrows. VP40E-I307R, which exclusively forms rings, does not migrate to the membrane but rather forms perinuclear structures.

(D) EM micrographs show that WT-VP40E and VP40E-R134A cause typical membrane ruffling, assembly, and budding of filamentous VLPs (black arrows). VP40E-M241R displays an exaggerated wild-type VP40 membrane-ruffling morphology, yet the cell surface remains devoid of budding filamentous VLPs. VP40E-I307R and VP40E-R134A/I307R display no membrane ruffling, matrix assembly, or budding activity. Solid scale bars, 1 μm; dashed scale bars, 500 nm. See also Figures S3 and S4.

Residue Q309 is in close proximity to I307 but is solvent exposed like T242, rather than buried in the CTD-to-CTD interface. As expected, cells transfected with VP40E-Q309R assemble and bud ebolavirus VLPs at wild-type levels (Figure 3B).

A different VP40 mutation, R134A, has been previously shown to eliminate binding of RNA, disrupt formation of VP40 rings, and yield wild-type VLP morphologies and levels of budding (Hoenen et al., 2005). Here, we show that purified VP40EΔN-R134A remains a dimer and confirm that VP40E-R134A assembles and buds VLPs at wild-type levels (Figures 3 and S1). We next generated a double mutant, VP40E-R134A/I307R, in which the I307R component would prevent CTD-mediated filament assembly and the R134A component would prevent I307R-induced RNA binding and ring formation. As anticipated, purified VP40EΔN-R134A/I307R mutant is a nucleic-acid-free dimer in solution ($A_{260/280} < 0.6$) (Figure S1). When transfected, VP40E-R134/I307R no longer forms perinuclear inclusions. Instead, it migrates to the cellular membrane, consistent with a dimeric VP40 phenotype (Figure 3C). Although VP40E-R134A/I307R is a membrane-trafficking dimer, it does not assemble or bud VLPs (Figure 3), consistent with disruption of the CTD-to-CTD interface by I307R. However, unlike cells transfected with VP40E-M241R, cells transfected with VP40E-R134A/I307R are devoid of membrane ruffles (Figure 3D). Modeling suggests that, unlike M241R, the VP40E-I307R point mutation would strictly prohibit any CTD-to-CTD interactions. Thus, the lack of membrane ruffling is likely due to the inability of dimeric VP40E-R134A/I307R to further assemble via the CTD along the membrane.

Taken together, these results indicate that targeted mutations to the CTD-to-CTD interface (M241R and I307R) block matrix assembly and budding, whereas similar control mutations to nearby residues in the CTD not directly involved in the CTD-to-CTD interface (T242R and Q309R) have no effect on matrix assembly and budding. Thus, the CTD-to-CTD interface, by which VP40 dimers further assemble into filaments, appears essential for matrix assembly and budding. In contrast, the RNA-binding ring structures formed by VP40E-I307R do not migrate to the membrane, assemble the viral matrix, or bud VLPs. Currently, how the I307R mutation triggers VP40 ring formation or how wild-type VP40 transitions into a ring during infection remain unknown.

## A Conserved Basic Patch in the VP40 CTD Is Essential for Assembly and Budding of Virus-like Particles

It has been previously shown that the C-terminal domain of VP40 is essential for electrostatic membrane interactions (Ruigrok et al., 2000). We hypothesized that basic residues in the CTDs of VP40 dimers were likely important for interacting with the negatively charged cytoplasmic leaflet of the cell membrane. We identified a basic surface on the VP40 CTD that is uniformly exposed on a single side of the VP40 dimer surface (Figure 4A). This basic patch is composed of six lysine residues (K221, K224, K225, K270, K274, and K275) and is conserved across the five distinct ebolaviruses (K225 is the one exception; it is R225 in Bundibugyo virus). We first targeted K224 and K225, as they reside in a flexible ten-residue loop that projects out from the CTD basic patch (disordered in all crystal structures of VP40). Initially, we deleted the loop entirely, generating the mutant VP40E-Δ221-229, and found that although expression levels and the dimeric structure were maintained, budding was abrogated (Figures S1 and S5). We next returned only the residues 223–226 (GKKG), generating VP40E-ΔGKKGΔ, in which residues 221–222 and 227–229 remained deleted. The restoration of just the GKKG component to VP40 restored wild-type budding activity (Figure 4C). To determine whether it was the electrostatic charge of the KK motif that was important, we generated three mutants: VP40E-ΔGMMGΔ (neutral charge, similar in structure to lysine), VP40E-ΔGEEGΔ (negative charge), and VP40E-ΔGRRGΔ (positive charge). Only cells transfected with VP40 containing positively charged residues at positions 224 and 225 were able to efficiently assemble and bud VLPs (Figure 4). By contrast, cells transfected with VP40-ΔGEEGΔ or VP40-ΔGMMGΔ display a failure to properly interact with the membrane or bud VLPs (Figures 4C and 4D). These results suggest that the positive charge in positions 224 and 225 of the GKKG-containing loop is essential to proper membrane interactions, matrix assembly, and budding of virus-like particles.

To further confirm the involvement of this CTD basic patch in assembly, we mutated a second pair of conserved basic residues, K274 and K275, to yield VP40E-K274R/K275R (conserves positive charge) and VP40E-K274E/K275E (replaces with negative charge). As anticipated, VP40E-K274R/K275R buds at wild-type levels, whereas VP40E-K274E/K275E fails to bud any VLPs (Figure 4B). Interestingly, in contrast to VP40E-ΔGMMGΔ and VP40E-ΔGEEGΔ, VP40E-K274E/K275E clearly interacts with the cell membrane (Figure 4C) while displaying no matrix assembly activity at the cell surface (Figure 4D). The absence of any membrane ruffling by VP40E-K274E/K275E, in contrast to VP40E-M241R (Figure 3D), suggests that electrostatic interactions of VP40 with the cellular membrane may trigger a critical step in VP40 matrix assembly. This mechanism, which involves further VP40 oligomerization upon interaction with the membrane to drive matrix assembly and VLP budding, is consistent with previously published work (Adu-Gyamfi et al., 2013; Scianimanico et al., 2000).

Together, these results indicate that the conserved CTD basic patch is essential to membrane interactions and for triggering assembly of VP40 into the viral matrix to bud nascent virions. Additionally, the importance of the CTD basic surface indicates the most probable orientation and surface by which dimeric VP40 interacts with the cellular membrane.

## A Crystal Structure of Hexameric VP40 Reveals How Dimers May Further Assemble into the Viral Matrix

It has previously been shown that VP40 undergoes conformational change at the plasma membrane, involving separation of the N- and C-terminal domains (Adu-Gyamfi et al., 2013; Gomis-Rüth et al., 2003; Scianimanico et al., 2000). Here, we have shown that the NTD-to-NTD interface that assembles the native VP40 dimer and the CTD-to-CTD interface by which dimers further assemble are both essential for matrix assembly and budding. However, these crystal structures were determined in the absence of phospholipids or electrostatically negative mimics. Although these structures display the dimeric interface, the CTD-CTD interface, and the basic surface that

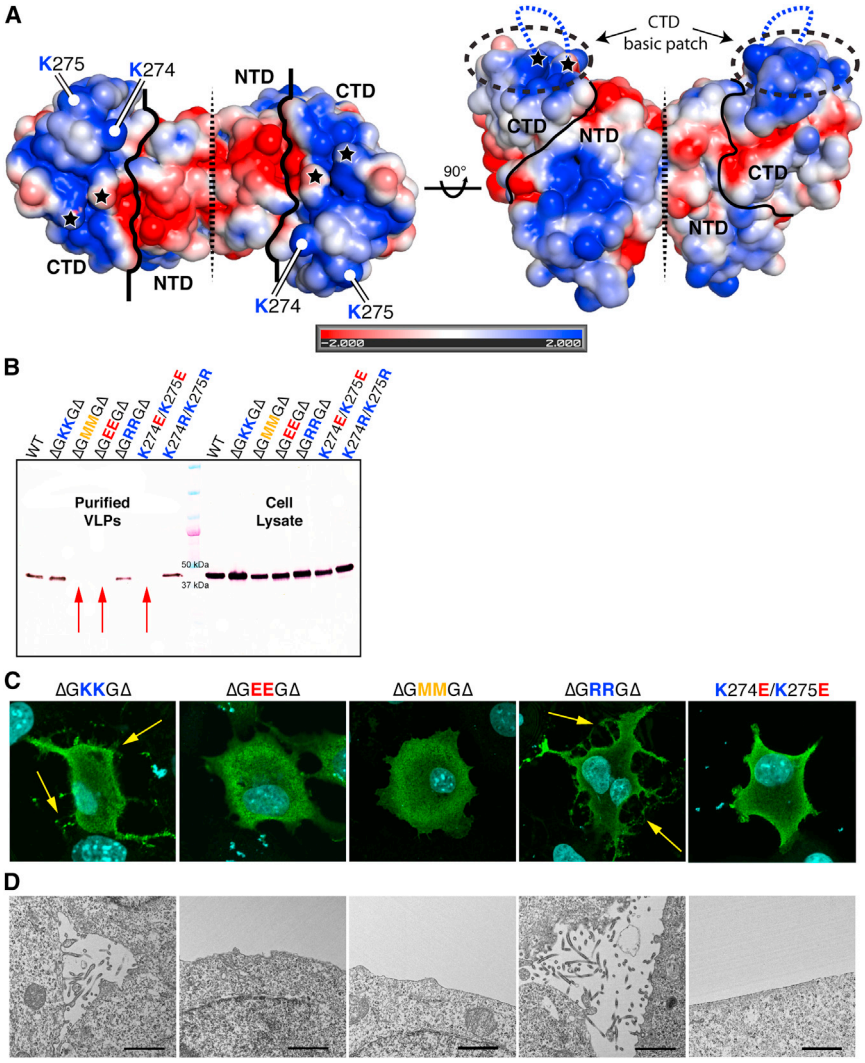


**Figure 4. Characterization of VP40 Basic Patch**

(A) Electrostatic surface potential of the VP40EΔN dimer in two orientations. The dimer interface is indicated by a dashed line, and the division of the NTD and CTD is depicted by a solid black line. The attachment points of the disordered GKKG loop are indicated by stars, and the loop is modeled as a broken blue line (on right).

(B) Western blot of cell lysates and purified VLPs from transfected cells. The VP40E-ΔGMMGΔ, VP40E-ΔGEEGΔ, and VP40E-K274E/K275E constructs express, but fail to assemble or bud VLPs (red arrows).

(C) IFA demonstrates that VP40E-ΔGKKGΔ and VP40E-ΔGRRGΔ assemble and bud VLPs (yellow arrows). By contrast, VP40E-ΔGEEGΔ and VP40E-ΔGMMGΔ do not interact as well with membrane and do not bud VLPs. Whereas VP40E-K274E/K275E clearly migrates to and interacts with the cell membrane, it fails to assemble and bud VLPs.

(D) EM micrographs display active VLP assembly and budding for VP40E-ΔGKKGΔ and VP40E-ΔGRRGΔ but no assembly or VLP budding for VP40E-ΔGEEGΔ, VP40E-ΔGMMGΔ, or VP40E-K274E/K275E. Scale bars, 500 nm.

See also Figure S5 and Movie S1.

are all critical to matrix assembly (Figures 2, 3, and 4), they do not account for the rotation of the CTD away from the NTD that is thought to occur at the cell membrane (Gomis-Rüth et al., 2003; Scianimanico et al., 2000). We wondered how electrostatic interactions with the membrane would affect VP40 structure and assembly. Thus, we made a series of attempts to electrostatically satisfy the positively charged elements of the CTD basic patch by screening crystal conditions in the presence of various negatively charged additives. We found success when using dextran sulfate (Mr = 5 kDa) as an additive. Of particular relevance, negatively charged dextran sulfate has been shown to outcompete binding of similarly charged phosphatidylserine, a known ligand of VP40 in the cell membrane (Ruigrok et al., 2000; Zschörnig et al., 1993).

VP40EΔN crystals grown in the presence of dextran sulfate belong to the space group $P42_12$ and diffract to 3.5 Å with three VP40 protomers (one and a half dimers) in the ASU. A crystallographic 2-fold axis lies along the VP40 dimer interface, joining the "half dimer" at the end of one ASU to the "half-dimer" at the start of the neighboring ASU to assemble a complete dimer. Thus, the biologically relevant unit present in these crystals is a hexameric structure comprised of three VP40 dimers (Figure 5). At each end of the hexamer is a VP40 protomer with its NTD and CTD in similar arrangement to those previously crystallized (Figure 5A). The remaining four VP40 protomers in the center of the hexamer have undergone conformational changes that have separated their N- and C-terminal domains. The NTDs of these four protomers derive the central core of the hexamer and assemble through an interface that we refer to as the "oligomerization interface" (Figure 5A). This oligomerization interface is homologous to the "antiparallel dimer" interface previously observed in the context of the VP40 RNA-binding ring crystal structure (Gomis-Rüth et al., 2003). The oligomerization interface is centered on residue W95 and is revealed only through conformational displacement of the CTD away from the NTD (Figure 5B). After the conformational changes, the four CTDs extend out from the central core VP40 protomers in opposing directions (half are "up" and half are "down"). Electron density for the central core VP40 protomers is only observable for the NTDs, as the "sprung" CTDs linked to these NTDs now extend into large solvent channels in the crystal packing and are disordered (Figure 5C). In the crystal, the VP40 hexamers also further assemble into uninterrupted filamentous structures via the same CTD-to-CTD interface described above (Figure 3), through the "unsprung" CTDs of adjacent ASUs (Figure 5C).

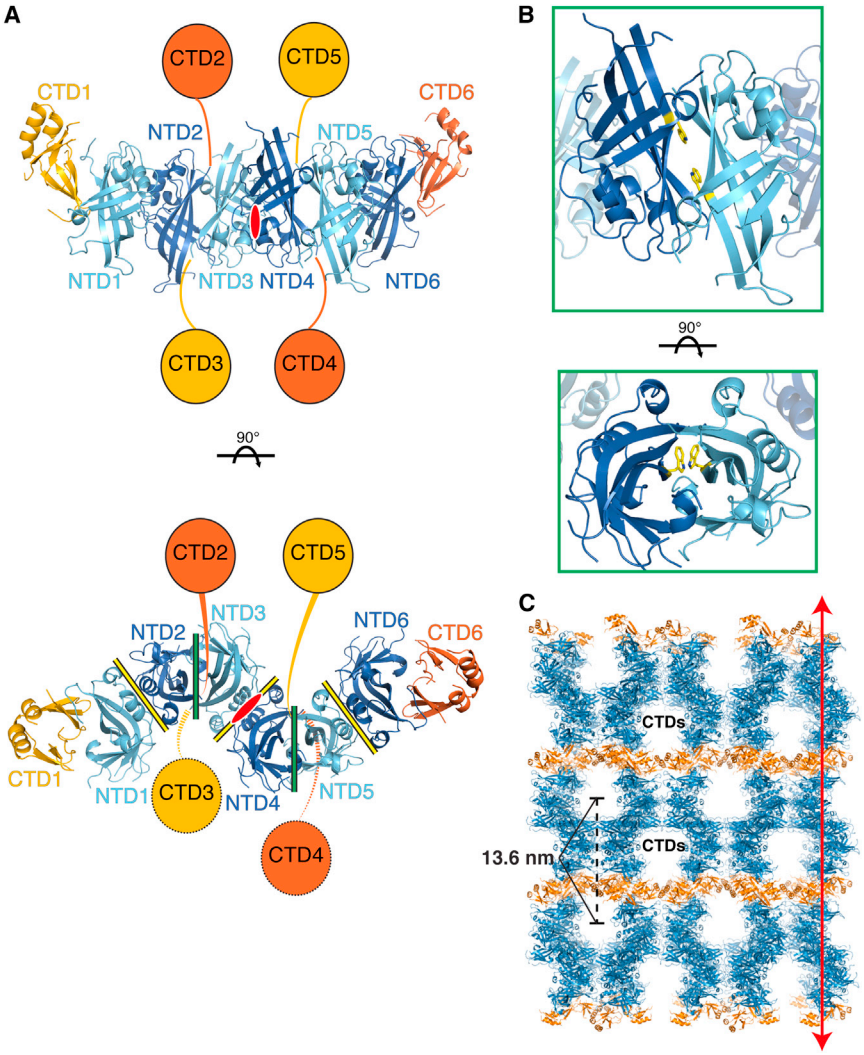


**Figure 5. Hexameric VP40 Crystal Structure**

(A) The VP40EΔN hexamer structure assembled across a crystallographic 2-fold axis (red oval) is illustrated with the NTDs alternating in colors of light or dark blue, and the CTDs alternate in light or dark orange. The NTDs and CTDs are numbered according to the protomer to which they belong. The disordered "sprung" CTDs are modeled as circles (to scale). Below: a 90° rotation in which the dimeric and oligomeric interfaces are indicated by yellow and green lines, respectively.

(B) The oligomerization interface is displayed from the VP40 hexamer and is centered on residue W95 (yellow).

(C) A section of the VP40EΔN hexamer crystal packing is shown; the NTD is colored blue; and the CTD is colored orange. Here, the uninterrupted filament structures formed via the CTD-to-CTD interface (one filament indicated by a red line) as well as the large solvent channels that contain the "sprung" CTDs can be seen.

The observed filaments assembled from the VP40 hexamer provide a compelling model for ebolavirus matrix assembly, as they combine all of the biologically relevant VP40 surfaces and interfaces shown to be critical to matrix assembly: (1) the NTD-to-NTD dimeric interface involving L117 and T112 (Figure 2), (2) the CTD-to-CTD interface involving M241 and I307 (Figure 3), (3) the conserved membrane-interacting CTD basic patches oriented along one single surface of the assembled filament (Figures 4 and S6), and (4) the "oligomerization interface," by which the NTDs assemble the central core of the hexamer (Hoenen et al., 2010a).

## The RNA-Binding VP40 Octameric Ring Plays a Distinct Role in the Viral Life Cycle

Previous work demonstrated that VP40 is capable of assembling an RNA-binding ring and that binding of RNA by VP40 is vital to the ebolavirus life cycle (Gomis-Rüth et al., 2003; Hoenen et al., 2005). Previous work also suggested that RNA may be essential to forming or maintaining the VP40 ring structure (Timmins et al., 2003). Here, however, we obtained a crystal structure of an RNA-free octameric VP40 ring. This RNA-free ring resulted from degradative loss of the CTDs within a crystal drop that originally contained purified RNA-free ($A_{260/280}$ < 0.6), dimeric VP40EΔN (Figure 6). These crystals belong to the space group P422 and diffract to 1.85 Å. The RNA-free ring is nearly identical to the previously determined RNA-bound ring (Gomis-Rüth et al., 2003), and both are assembled by the same interfaces: the oligomerization interface, also observed in the VP40 hexamer, and another interface unique to the VP40 ring structure, which we term the "RNA-binding interface" (Figure 6A).

The RNA-free ring structure demonstrates that RNA is not structurally necessary to stabilize or assemble the VP40 ring. However, in order to verify whether RNA-free VP40 rings can assemble outside of a crystal, we generated two VP40 CTD deletion constructs: VP40EΔCTD and VP40EΔCTD-R134A. Purified VP40EΔCTD binds RNA ($A_{260/280}$ > 1.0) and displays a size-exclusion chromatography elution profile consistent with formation of oligomeric rings in solution and with previous work (Gomis-Rüth et al., 2003). The R134A point mutation prevents RNA binding, and as anticipated, purified VP40EΔCTD-R134A is RNA-free ($A_{260/280}$ < 0.6). However, its size-exclusion profile is consistent with that of VP40EΔCTD, demonstrating formation of RNA-free rings in solution (Figure S1). Taken together, RNA is likely critical to the displacement of the CTD from the NTD to trigger assembly of the ring structure and is not necessary for the stability of the NTD-formed ring structure itself.

There is one consistent structural difference that appears to be critical to the formation of the VP40 octamer versus the VP40 dimer and hexamer. As observed both here and previously (Gomis-Rüth et al., 2003), the N-terminal 69 residues of VP40 need to move out of the dimeric interface in order for ring formation

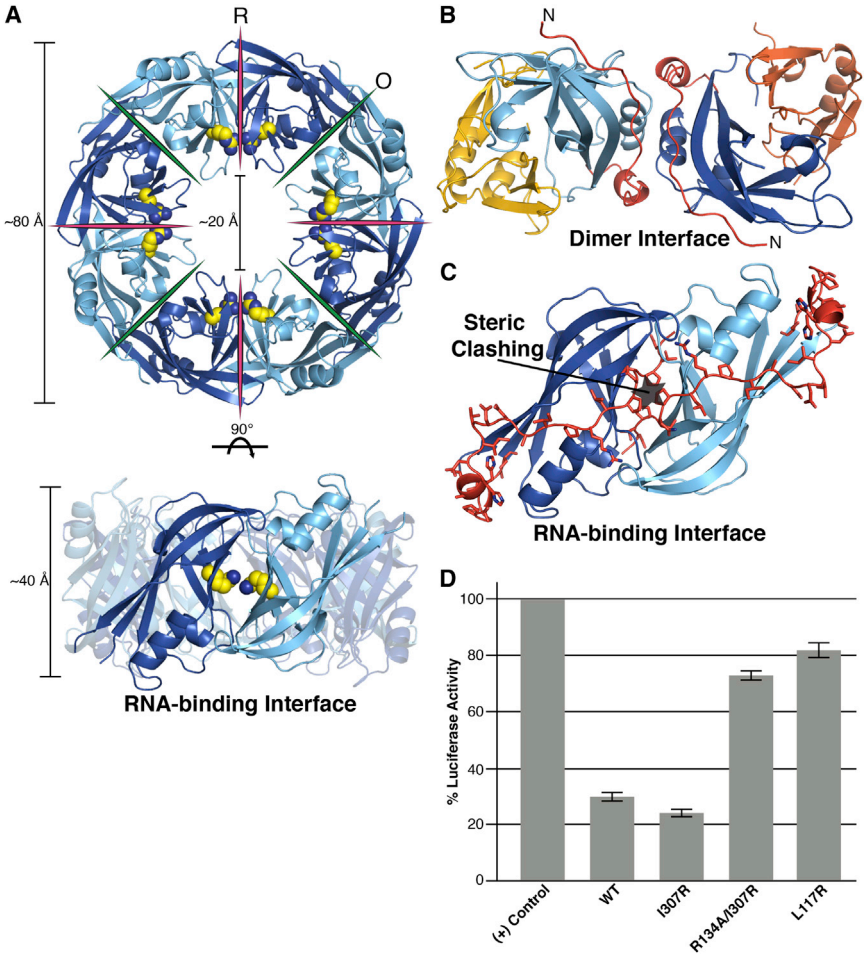


**Figure 6. Analysis of the Octameric VP40 Ring Structure**

(A) Crystal structure of the RNA-free VP40 octameric ring, with alternating NTD protomers colored in light and dark blue. Residue R134 is depicted by yellow spheres. The oligomeric interface and RNA-binding interface are indicted by green and pink lines, respectively.

(B) The VP40EΔN dimer. Opposing NTDs are colored light or dark blue, and the CTDs are colored light or dark orange. Residues 45–70 in the dimer interface are colored red.

(C) By alignment of the NTDs from dimeric VP40 and RNA-bound VP40, we have modeled residues 45–70 ordered in the dimer (red) onto the RNA-binding interface. The alignment demonstrates how assembly of the RNA-binding interface would be obstructed unless residues 1–70 unraveled from the NTD structure.

(D) Minigenome reporter assays were performed in triplicate, and data were normalized to a positive control, expressing Renilla Luciferase to reflect transcription levels of 100%. WT-VP40E reduces transcription by ~70%. Error bars represent the SD of 3.7%, and VP40E-I307R reduces transcription by ~80% (SD = 2.6%). In contrast, VP40E-R134A/I307R and VP40E-L117R only reduce levels of transcription by ~30% (SD = 3.3%) and ~20% (SD = 5.3%), respectively.

See also Movie S2.

to occur (Figure 6B). This conformational change likely destabilizes the dimeric interface and exposes the RNA-binding interface (Figure 6C). Importantly, previous work—showing the presence of VP40 rings in ebolavirus-infected cells (Gomis-Rüth et al., 2003)—and our full-length VP40E-I307R mutant, which exclusively assembles VP40 rings, demonstrate that these conformational changes also occur in the context of full-length VP40.

The precise role of the VP40 RNA-binding ring in the viral life cycle has yet to be elucidated. Data presented here indicate that ring-forming VP40 does not traffic to the membrane and is not required to bud VLPs (Figure 3). It has been suggested that the RNA-binding VP40 ring likely has a critical role outside virion assembly (Gomis-Rüth et al., 2003; Hoenen et al., 2005), possibly in negative regulation of viral transcription (Hoenen et al., 2010b). The discovery that our VP40E-I307R mutant exclusively assembles into rings allows us to unambiguously study the function of the full-length VP40 ring oligomer in the cell using ebolavirus minigenome reporter assays (Figure 6D). Consistent with previous studies, we find WT-VP40E reduces transcription by ~70% compared to our normalized control (Hoenen et al., 2010b). Further, we find our VP40E-I307R ring-only mutant reduces viral transcription by ~80%. Thus, VP40 locked into the ring structure can entirely recapitulate the transcriptional control function. Next, to determine whether RNA binding by VP40 is critical to the observed reduction in transcription, we repeated the experiment with a double mutant incapable of RNA binding, VP40E-R134A/I307R, and only observed a ~30% reduction in transcription signal. Therefore, the RNA-binding activity of the VP40 ring structure is critical to the regulation of viral transcription observed with WT-VP40E and VP40E-I307R.

Because regulation of viral transcription is not directly linked to the dimeric structure of VP40, we were able to use the monomeric VP40E-L117R mutant to test whether dimeric VP40 is the precursor structure to the RNA-binding ring. If VP40 exists as a monomeric precursor, then assembly of the RNA-binding VP40 ring should still occur (L117R would be surface exposed in both monomer and ring), resulting in wild-type VP40 levels of transcriptional regulation. However, VP40E-L117R displays only an ~20% reduction in viral transcription, suggesting that dimeric VP40 is a necessary precursor to binding of RNA and assembly of the VP40 RNA-binding ring. This result is in agreement with a previous study suggesting that dimeric VP40 may be a building block of higher-molecular-weight oligomers (Timmins et al., 2003).

In summary, the results here show that the VP40 ring structure has a clear role in regulation of viral transcription through its RNA-binding activity, a role that is critical to the ebolavirus life cycle (Hoenen et al., 2005). Additionally, dimeric VP40 is an

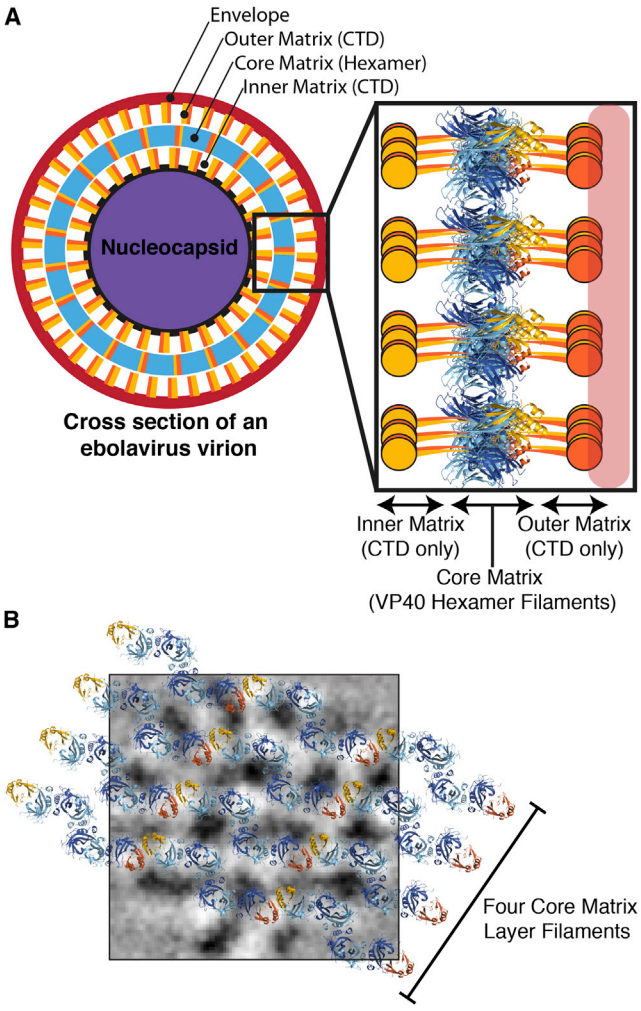


**Figure 7. Model of the VP40 Matrix**

(A) A cross-section of an ebolavirus virion is modeled by assembly of VP40 (NTD is colored blue; CTD is colored light or dark orange) into a multilayered matrix as predicted by our hexameric crystal structure and by tomographic studies (Beniac et al., 2012; Bharat et al., 2011). The black box on the cross-section corresponds to the box at right containing a four-filament assembly. In this model, the crystal structure of the hexamer-assembled filament forms the core layer of the matrix. The basic patches of the hexamer CTDs are positioned toward the outer membrane, and the "sprung" CTDs form the inner and outer matrix layers.

(B) Four individual VP40 filaments derived from the assembly of VP40 hexamers are modeled to scale onto 2D averages of virion tomograms. Black/white has been inverted for clarity in these images; white now corresponds to VP40 density (adapted from Beniac et al., 2012).

See also Figure S6.

important precursor not only to matrix assembly but also to binding of RNA and assembly of the VP40 RNA-binding ring.

## DISCUSSION

How VP40 assembles the viral matrix and achieves its multiple roles in the ebolavirus life cycle has remained enigmatic. We discovered that VP40 is not a monomer, but is instead dimeric and that the dimeric structure of VP40 is a critical precursor to matrix assembly and budding.

The VP40 dimer structure has a butterfly-like shape with a conserved basic patch in the CTD that is exposed across a single surface of the dimer. Removing the positive charge of residues contained in the CTD basic patch abrogates assembly and budding of VLPs. The essential nature of this patch, coupled with the absence of a uniformly presented basic surface anywhere else on the VP40 dimer, suggests that the surface containing the CTD basic patches likely interacts with the negatively charged cytoplasmic leaflet of the cellular membrane. Interestingly, our basic patch mutants display different phenotypes in our IFA experiments. The VP40-ΔGEEGΔ mutant appears to migrate out from the nucleus toward the membrane but fails to interact with the membrane, whereas the VP40E-K274E/K275E mutant very clearly interacts with the cellular membrane. We hypothesize that the projecting VP40 GKKG loop is likely critical to initial interactions with and orientation of VP40 to the membrane. We further hypothesize that, as the VP40 dimer aligns along the membrane, residues K274 and K275 contact lipid and trigger conformational changes needed to assemble the viral matrix and bud nascent virions. This model is consistent with previously reported data (Adu-Gyamfi et al., 2012; Ruigrok et al., 2000; Scianimanico et al., 2000) and our micrographs formed by electron microscopy (EM) that display a membrane-ruffling phenotype with VP40E-M241R, but not with VP40E-K274E/K275E. These observations suggest that electrostatic interactions between the VP40 dimer and the membrane trigger a step in viral matrix assembly.

We also showed that cocrystallization of VP40 with dextran sulfate, a 5 kDa electrostatically negative mimic of the known VP40 membrane ligand phosphatidylserine (Ruigrok et al., 2000), triggers VP40 conformational rearrangements and assembly of VP40 dimers into a linear hexameric structure (Figure 4). The process by which the VP40 hexamer structure assembles likely involves multiple steps: (1) dimeric VP40 migrates to the membrane and interacts along the membrane in a uniform fashion via the basic patches on the CTDs, (2) VP40 dimers then begin to assemble with each other through CTD-to-CTD interactions, and (3) a twisting motion is induced, springing the CTD away from NTD to facilitate the antiparallel assembly of VP40 dimers along the oligomerization interface observed in the VP40 hexamer (Movie S1). Recently, VP40 was shown to partially penetrate the cell membrane upon matrix assembly (Adu-Gyamfi et al., 2013). A twisting motion could lend the force needed to push the CTD into the cell membrane.

In crystals, the VP40 hexamers assemble into continuous filaments via the conserved M241- and I307-containing CTD-CTD interface (Figures 7 and S6). In this arrangement, hexameric VP40 creates a filamentous multilayered assembly. A central or core layer is derived from repeating VP40 hexamers. Two other layers, sandwiching the core, are formed by the CTDs that spring up or down from the four NTDs at the core of each hexamer. We believe this arrangement may reflect how the filovirus matrix is assembled. CTDs of VP40 are known to interact with both the membrane on the outside of the virion and also the nucleocapsid at the center of the virion. The crystal structure, in which CTDs spring alternately up or down, explains how this could occur.

The "upper" layer of CTDs could interact with the viral membrane, whereas the "lower" layer of CTDs could interact with the viral nucleocapsid (Figure 7A).

Recent tomographic analysis of filovirus virions demonstrates that VP40 indeed assembles into a multilayered matrix (Bharat et al., 2011), reflected in our model. In tomography, density for the outer layer may have merged a bit with the membrane; as in biophysical studies, the CTDs are observed to partially penetrate the membrane. In tomography, a "space" between the core matrix layer is observed; in our model, the N-terminal domains of the hexamer-assembled core do not lie directly against the membrane after conformational changes have occurred (Beniac et al., 2012; Bharat et al., 2011). Rather, the outer layer is bridged to the core layer by the flexible linkers of the CTDs, which are not electron dense.

Further, as observed in tomographic studies, repeating structural features along the axis of the virion closely correspond to repeating features observed in the VP40 hexamer: ~5 nm (width of NTD dimer) and ~7 nm (length of repeating ASUs in hexamer-assembled filaments) (Beniac et al., 2012; Bharat et al., 2011). Tomographic two-dimensional (2D) averages of the VP40 matrix from ebolavirus suggest that the matrix has a somewhat flexible and pleomorphic, but generally repeating structure (Beniac et al., 2012). Individual VP40 filaments assembled by repeating hexamers in the crystal packing match the observed repeating density array in 2D averages from equivalent tomographic slices (Figure 7B).

A remaining question is whether, in the actual viral matrix, all CTDs have sprung and the central core is made only from NTDs or whether the central core layer is assembled from repeating hexamers at each end. We believe that CTD-CTD interactions are likely involved in the core matrix layer. Only the CTD-CTD interface provides a slippery, flexible surface. All NTD-NTD interfaces visualized thus far are rigid. An NTD-only filament, in the absence of any CTD-CTD interfaces contained at any interval within it, would likely present a rigid, uniform structure, inconsistent with the flexible and pleomorphic nature of the filovirus virion (Bharat et al., 2011; Beniac et al., 2012). Further, our mutagenesis to the CTD (Figure 3) and previous work demonstrating lipid-induced assembly of VP40 hexamers (Scianimanico et al., 2000) suggest that CTD-to-CTD interactions and discrete hexameric units, as are bounded by this interaction, are both critical parts of the ebolavirus matrix structure.

Until now, the roles of RNA binding and the resulting VP40 ring structures in the viral life cycle have remained elusive. This was primarily due to the fact that studying VP40 ring formation in the cell has previously required either truncating the CTD or utilizing mutations that we now see affect all of dimer, octamer, and hexamer. Here, the I307R mutation allowed us to unambiguously characterize the cellular function of full-length VP40 in its oligomeric ring state. We found that when VP40 is bound to RNA and adopts the ring structure, it assumes a perinuclear location. Moreover, our minigenome assays now demonstrate that binding of RNA by VP40 and the RNA-binding ring structure confer the transcriptional control function. Recent studies demonstrate that in the early stages of ebolavirus infection, VP40 first participates in the formation of perinuclear structures with additional viral proteins (Nanbo et al., 2013). Thus, we propose that VP40 RNA binding is critical to the initial stages of viral transcription upon infection. This is consistent with previous data that indicate recombinant viruses with a VP40 RNA-binding knockout mutation (R134A) fail to replicate (Hoenen et al., 2005). The mechanism by which VP40 transitions from a dimer to a ring structure during an infection remains elusive and is the topic of continued investigation. Although RNA is not required to form a ring from CTD-deleted VP40, it may play a role in displacement of NTD and CTD from each other in natural infection. A hypothesis for how dimeric VP40 transitions into the ring structure is modeled in Movie S2.

The results presented here and previously (Timmins et al., 2003) illustrate how the VP40 protein performs multiple distinct roles in the ebolavirus life cycle. Through structural rearrangements, VP40 assembles multiple distinct structures with unique and essential functions. It is known that viral proteins are multifunctional, but our work on VP40 calls into question the belief that a single viral protein structure or assembly is responsible for all of the known functions of that protein. Viruses, particularly RNA viruses, can be subject to limitations on genomic size. By encoding proteins that can structurally rearrange themselves to operate at different stages of the life cycle, viruses like the ebolaviruses can accomplish a multitude of essential functions with a limited number of genes. Further, other viral matrix proteins, such as M of respiratory syncytial virus and M1 of influenza virus, are also constructed via discrete NTDs and CTDs connected by a long linker, bind RNA, and regulate viral transcription (Baudin et al., 2001; Money et al., 2009). Hence, other viruses may encode proteins capable of similar structural transformations.

The structure-shifting properties of VP40 provide additional opportunities for the development of antiviral drugs. For example, small molecules capable of influencing the propensity of one VP40 structure over another (as seen with VP40E-I307R) could severely impede the ebolavirus life cycle. VP40 thus provides a model for how viruses with small genomes, like ebolaviruses, can accomplish a multitude of essential functions with a limited number of proteins.

## EXPERIMENTAL PROCEDURES

### Protein Expression and Purification

VP40SΔN and VP40EΔN (and VP40EΔN mutants) were expressed in BL-21 Rosetta 2 *Escherichia coli* cells using the pET-46 Ek/LIC vector. For details, see the Extended Experimental Procedures.

### Western Blots

293 cells were transfected with a pTRIEX 5 plasmid expressing WT-VP40E or a mutant VP40E. Analysis was carried out 24 hr posttransfection. For details, see the Extended Experimental Procedures.

### Confocal Microscopy

293 cells were transfected with a pCAGGS plasmid expressing WT-VP40E or a mutant VP40E. Analysis was carried out 24 hr posttransfection. For additional details, see the Extended Experimental Procedures.

Other methods are described in the Extended Experimental Procedures.

## ACCESSION NUMBERS

Coordinates and structure factors have been deposited into the Protein Data Bank under the accession codes 4LD8, 4LDB, 4LDD, 4LDI, and 4LDM.

## SUPPLEMENTAL INFORMATION

Supplemental Information includes Extended Experimental Procedures, six figures, one table, and two movies and can be found with this article online at http://dx.doi.org/10.1016/j.cell.2013.07.015.

## ACKNOWLEDGMENTS

We thank the beamline scientists at APS 19-ID and GM/CA 23-ID, SSRL 12-2, and ALS 5.0.2, Dr. Jean-Philippe Julien for assistance with the SEC-MALS analysis, Christina Corbaci for the Graphical Abstract, and Drs. Glen Nemerow and B.V.V Prasad for helpful comments and suggestions. E.O.S. was supported by a Career Award in the Biomedical Sciences and an Investigator in the Pathogenesis of Infectious Disease Award from the Burroughs Welcome Fund, as well as The Skaggs Institute of Chemical Biology and a National Institute of Allergy and Infectious Disease award (R43 AI1088843). Z.A.B. was supported by a grant (2T32AI007244) to the TSRI Department of Immunology and Microbial Science. Y.K. acknowledges membership within and support from the Region V "Great Lakes" Regional Center for Excellence (RCE) for Biodefense and Emerging Infectious Disease Research Program (National Institutes of Health award [U54 AI057153]). T.N. was supported by a Grant-in-Aid for Young Scientists from the Japan Society for the Promotion of Science and by a Grant-in-Aid for Scientific Research on Priority Areas from the Ministry of Education, Culture, Sports, Science, and Technology. This is manuscript #21649 from The Scripps Research Institute.

Received: February 20, 2012
Revised: May 13, 2013
Accepted: July 12, 2013
Published: August 15, 2013

## REFERENCES

Adams, M.J., and Carstens, E.B. (2012). Ratification vote on taxonomic proposals to the International Committee on Taxonomy of Viruses. Arch. Virol. *157*, 1411–1422.

Adu-Gyamfi, E., Digman, M.A., Gratton, E., and Stahelin, R.V. (2012). Investigation of Ebola VP40 assembly and oligomerization in live cells using number and brightness analysis. Biophys. J. *102*, 2517–2525.

Adu-Gyamfi, E., Soni, S.P., Xue, Y., Digman, M.A., Gratton, E., and Stahelin, R.V. (2013). The Ebola virus matrix protein penetrates into the plasma membrane: a key step in viral protein 40 (VP40) oligomerization and viral egress. J. Biol. Chem. *288*, 5779–5789.

Baudin, F., Petit, I., Weissenhorn, W., and Ruigrok, R.W. (2001). In vitro dissection of the membrane and RNP binding activities of influenza virus M1 protein. Virology *281*, 102–108.

Beniac, D.R., Melito, P.L., Devarennes, S.L., Hiebert, S.L., Rabb, M.J., Lamboo, L.L., Jones, S.M., and Booth, T.F. (2012). The organisation of Ebola virus reveals a capacity for extensive, modular polyploidy. PLoS ONE *7*, e29608.

Bharat, T.A., Riches, J.D., Kolesnikova, L., Welsch, S., Krähling, V., Davey, N., Parsy, M.L., Becker, S., and Briggs, J.A. (2011). Cryo-electron tomography of Marburg virus particles and their morphogenesis within infected cells. PLoS Biol. *9*, e1001196.

Bwaka, M.A., Bonnet, M.J., Calain, P., Colebunders, R., De Roo, A., Guimard, Y., Katwiki, K.R., Kibadi, K., Kipasa, M.A., Kuvula, K.J., et al. (1999). Ebola hemorrhagic fever in Kikwit, Democratic Republic of the Congo: clinical observations in 103 patients. J. Infect. Dis. *179*(*Suppl 1*), S1–S7.

Dessen, A., Forest, E., Volchkov, V., Dolnik, O., Klenk, H.D., and Weissenhorn, W. (2000a). Crystallization and preliminary X-ray analysis of the matrix protein from Ebola virus. Acta Crystallogr. D Biol. Crystallogr. *56*, 758–760.

Dessen, A., Volchkov, V., Dolnik, O., Klenk, H.D., and Weissenhorn, W. (2000b). Crystal structure of the matrix protein VP40 from Ebola virus. EMBO J. *19*, 4228–4236.

Geisbert, T.W., and Jahrling, P.B. (1995). Differentiation of filoviruses by electron microscopy. Virus Res. *39*, 129–150.

Gomis-Rüth, F.X., Dessen, A., Timmins, J., Bracher, A., Kolesnikowa, L., Becker, S., Klenk, H.D., and Weissenhorn, W. (2003). The matrix protein VP40 from Ebola virus octamerizes into pore-like structures with specific RNA binding properties. Structure *11*, 423–433.

Harty, R.N. (2009). No exit: targeting the budding process to inhibit filovirus replication. Antiviral Res. *81*, 189–197.

Harty, R.N., Brown, M.E., Wang, G., Huibregtse, J., and Hayes, F.P. (2000). A PPxY motif within the VP40 protein of Ebola virus interacts physically and functionally with a ubiquitin ligase: implications for filovirus budding. Proc. Natl. Acad. Sci. USA *97*, 13871–13876.

Hoenen, T., Volchkov, V., Kolesnikova, L., Mittler, E., Timmins, J., Ottmann, M., Reynard, O., Becker, S., and Weissenhorn, W. (2005). VP40 octamers are essential for Ebola virus replication. J. Virol. *79*, 1898–1905.

Hoenen, T., Biedenkopf, N., Zielecki, F., Jung, S., Groseth, A., Feldmann, H., and Becker, S. (2010a). Oligomerization of Ebola virus VP40 is essential for particle morphogenesis and regulation of viral transcription. J. Virol. *84*, 7053–7063.

Hoenen, T., Jung, S., Herwig, A., Groseth, A., and Becker, S. (2010b). Both matrix proteins of Ebola virus contribute to the regulation of viral genome replication and transcription. Virology *403*, 56–66.

Jasenosky, L.D., Neumann, G., Lukashevich, I., and Kawaoka, Y. (2001). Ebola virus VP40-induced particle formation and association with the lipid bilayer. J. Virol. *75*, 5205–5214.

Johnson, R.F., Bell, P., and Harty, R.N. (2006). Effect of Ebola virus proteins GP, NP and VP35 on VP40 VLP morphology. Virol. J. *3*, 31.

Kuhn, J.H. (2008). Filoviruses. A compendium of 40 years of epidemiological, clinical, and laboratory studies. Arch. Virol. Suppl. *20*, 13–360.

Kuhn, J.H., Becker, S., Ebihara, H., Geisbert, T.W., Jahrling, P.B., Kawaoka, Y., Netesov, S.V., Nichol, S.T., Peters, C.J., Volchkov, V.E., et al. (2011). Family *Filoviridae*. In Virus Taxonomy: Ninth Report of the International Committee on Taxonomy of Viruses. A.M.Q. King, M.J. Adams, E.B. Carstens, and E.J. Lefkowitz, eds. (London: Elsevier), pp. 665–671.

Money, V.A., McPhee, H.K., Mosely, J.A., Sanderson, J.M., and Yeo, R.P. (2009). Surface features of a Mononegavirales matrix protein indicate sites of membrane interaction. Proc. Natl. Acad. Sci. USA *106*, 4441–4446.

Nanbo, A., Watanabe, S., Halfmann, P., and Kawaoka, Y. (2013). The spatio-temporal distribution dynamics of Ebola virus proteins and RNA in infected cells. Sci. Rep. *3*, 1–9.

Noda, T., Sagara, H., Suzuki, E., Takada, A., Kida, H., and Kawaoka, Y. (2002). Ebola virus VP40 drives the formation of virus-like filamentous particles along with GP. J. Virol. *76*, 4855–4865.

Panchal, R.G., Ruthel, G., Kenny, T.A., Kallstrom, G.H., Lane, D., Badie, S.S., Li, L., Bavari, S., and Aman, M.J. (2003). In vivo oligomerization and raft localization of Ebola virus protein VP40 during vesicular budding. Proc. Natl. Acad. Sci. USA *100*, 15936–15941.

Ruigrok, R.W., Schoehn, G., Dessen, A., Forest, E., Volchkov, V., Dolnik, O., Klenk, H.D., and Weissenhorn, W. (2000). Structural characterization and membrane binding properties of the matrix protein VP40 of Ebola virus. J. Mol. Biol. *300*, 103–112.

Scianimanico, S., Schoehn, G., Timmins, J., Ruigrok, R.H.W., Klenk, H.D., and Weissenhorn, W. (2000). Membrane association induces a conformational change in the Ebola virus matrix protein. EMBO J. *19*, 6732–6741.

Timmins, J., Schoehn, G., Kohlhaas, C., Klenk, H.D., Ruigrok, R.W., and Weissenhorn, W. (2003). Oligomerization and polymerization of the filovirus matrix protein VP40. Virology *312*, 359–368.

Wyatt, P.J. (1998). Submicrometer particle sizing by multiangle light scattering following fractionation. J. Colloid Interface Sci. *197*, 9–20.

Zschörnig, O., Arnold, K., and Ohki, S. (1993). Effect of glycosaminoglycans and PEG on fusion of Sendai virus with phosphatidylserine vesicles. Biochim. Biophys. Acta *1148*, 1–6.

# Recycling rice husks for high-capacity lithium battery anodes

Dae Soo Jung[a,b,1], Myung-Hyun Ryou[a,1], Yong Joo Sung[c], Seung Bin Park[b], and Jang Wook Choi[a,2]

[a]Graduate School of Energy Environment Water Sustainability (World Class University) and KAIST Institute NanoCentury and [b]Department of Chemical and Biomolecular Engineering, Korea Advanced Institute of Science and Technology, Yuseong Gu, Daejeon 305-701, Korea; and [c]Department of Bio-Based Materials, Chungnam National University, Yuseong Gu, Daejeon 305-764, Korea

Edited by Stephen J. Harris, General Motors, Warren, MI, and accepted by the Editorial Board June 7, 2013 (received for review March 15, 2013)

**The rice husk is the outer covering of a rice kernel and protects the inner ingredients from external attack by insects and bacteria. To perform this function while ventilating air and moisture, rice plants have developed unique nanoporous silica layers in their husks through years of natural evolution. Despite the massive amount of annual production near $10^8$ tons worldwide, so far rice husks have been recycled only for low-value agricultural items. In an effort to recycle rice husks for high-value applications, we convert the silica to silicon and use it for high-capacity lithium battery anodes. Taking advantage of the interconnected nanoporous structure naturally existing in rice husks, the converted silicon exhibits excellent electrochemical performance as a lithium battery anode, suggesting that rice husks can be a massive resource for use in high-capacity lithium battery negative electrodes.**

Rice is one of the most widespread food crops for human sustenance (Fig. 1*A*). It is currently cultivated in about 75 countries, and more than one-third of the global population eats rice as a staple food. Its worldwide annual production amounts to ∼422 million metric tons (1). The cultivation of rice plants generates a waste product, so-called rice husks (RHs), and upon the complete harvest of rice, the content of the RH reaches ∼20 wt% of the entire rice kernel, a very large amount, considering the massive scale of global rice production. The utilization of RHs has been an extensive research topic for decades (2). However, practical applications of RHs have been limited to a narrow range of low-value agricultural items, such as fertilizer additives, stockbreeding rugs, and bed soil, because of their tough and abrasive properties (2). There is a large opportunity for further research targeting more valuable applications.

Although RHs contain a variety of components such as lignin, cellulose, and silica, the present study pays attention mainly to recycling of the silica component. It has been known (3, 4) that silica accounts for ∼15–20 wt% of the entire RHs (Fig. 1*B*, *Lower Inset*) and originates from monosilicic acid that is first introduced into rice plants through their roots and is then moved to the rigid outer epidermal walls of the plants where it is converted into silica. The silica in RHs plays an important role in protecting rice from external attack by insects and bacteria (3, 5, 6), but simultaneously facilitates ventilation between inside and outside RHs to preserve moisture and nutrients inside the kernels. To perform these critical dual functions, the silica in RHs has developed unique porous nanostructures through years of natural evolution.

In an effort to recycle RHs toward high-value applications, in the present investigation, the RH silica possessing unique nanostructures has been applied in high-capacity lithium ion battery (LIB) anodes by reducing the silica to silicon (Si). Si has recently attracted considerable attention as an LIB anode due to its unparalleled theoretical capacity around 4,000 mAh/g (7–9), which is about 10 times higher than that of conventional graphite anodes (∼370 mAh/g). The development of high-capacity Si anodes is expected to accelerate the emergence of more advanced hybrid electrical vehicles and portable electronic devices. Despite the promising feature associated with the high specific capacity, however, Si typically suffers from capacity fading during cycling. This severe drawback is attributed to the extraordinarily large volume change of Si alloys, up to 300% during charging and discharging processes. This leads to capacity-fading mechanisms such as fracture of the Si alloys (10, 11) and unstable solid electrolyte interphase (SEI) formation (12). By contrast, the RH-originated Si in the present study overcomes these issues by using its unique interconnected porous nanostructure. Even though a number of nanostructured Si materials have been demonstrated (13–15) as high-performance LIB anodes, the nanostructured Si from RHs is substantially different, for the naturally defined structures existing in living organisms are directly used. Moreover, the readily available amount (∼$10^7$ tons) (1) of the RH-originated Si from worldwide cultivation is at least several orders of magnitude larger than the current demand for LIB anode raw materials (∼$10^4$–$10^5$ tons) (16).

## Results and Discussion

The rice used in the current study was harvested from the suburbs of Daejeon in the Republic of Korea during September 2012. Characterization by optical microscopy reveals the morphology of RHs: The inner RH epidermis has a smooth surface, whereas the outer epidermis has a rough surface with repeated ridges (Fig. 1*B*, *Upper Inset*, and Fig. 1*C*). An elemental mapping analysis using energy dispersive spectroscopy (EDS) indicates that the silica is mainly concentrated at the tips of the outer surface (Fig. 1*C*, *Lower Inset* and Fig. S1). A more microscopic characterization of the concentrated silica region using scanning electron microscopy (SEM) showed that, in natural RHs, silica exists in the form of nanoparticles that are interconnected to constitute a porous structure (Fig. S1*B*). As summarized in Fig. 1*D*, during the overall synthetic procedure, the original RHs were first pretreated to extract high-purity silica, which was then reduced to generate the final Si. The detailed synthetic step and its yield are summarized in Fig. S2.

A thermal gravimetric analysis (TGA) verifies that silica indeed occupies 19.5 wt% of RHs (Fig. 2*A*). In the TGA data, the mass decreases in the temperature ranges of ∼175–350 °C and ∼380–550 °C correspond to decomposition of cellulose and lignin, respectively (17). In our experiment, we removed the 81.4 wt% of other organic and metal components through purification steps consisting of acid and heat treatments. Briefly, RHs were first leached with 10% (wt/vol) hydrochloric acid (HCl) and were then heat-treated at 650 °C for 3 h. See *Materials and Methods* for

Author contributions: D.S.J., S.B.P., and J.W.C. designed research; D.S.J. and M.-H.R. performed research; D.S.J., M.-H.R., and Y.J.S. analyzed data; and D.S.J., M.-H.R., and J.W.C. wrote the paper.

The authors declare no conflict of interest.

This article is a PNAS Direct Submission. S.J.H. is a guest editor invited by the Editorial Board.

[1]D.S.J. and M.-H.R. contributed equally to this work.

[2]To whom correspondence should be addressed. E-mail: jangwookchoi@kaist.ac.kr.

This article contains supporting information online at www.pnas.org/lookup/suppl/doi:10.1073/pnas.1305025110/-/DCSupplemental.

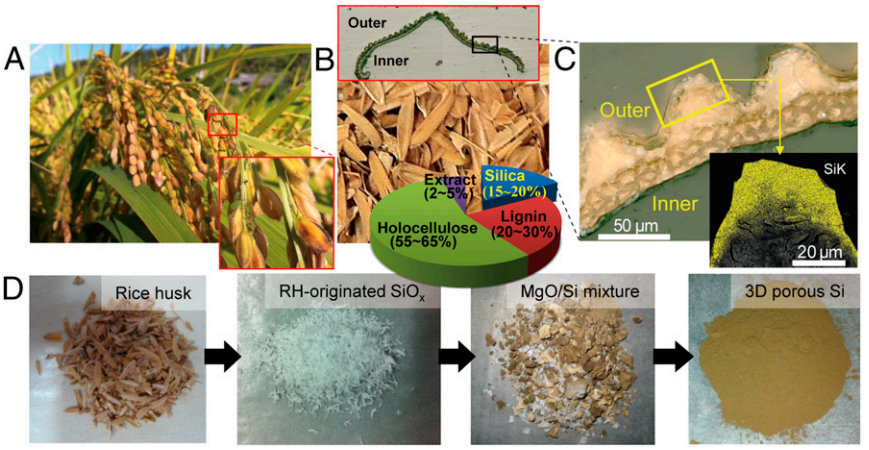


**Fig. 1.** Generation of 3D nanoporous Si from a rice plant. (*A*) Photographs of rice plant. (*B*) Photograph of rice husks obtained after milling. (*Upper Inset*) Optical microscope image showing the morphological characteristic of outer/inner surfaces of a rice husk. (*Lower Inset*) Circular chart indicating the composition of rice husks. (*C*) Optical microscope image of a rice husk shell magnified from the black box in *B*. (*Inset*) Si-mapped SEM-EDS image suggesting that Si exists mostly along the outer rugged surfaces of rice husks. (*D*) A series of photographs summarizing the procedures of synthesizing nanostructured Si from rice husks. (*Left* to *Right*) Pretreated rice husks by an acid-leaching process, rice husk-originated silica by a thermal decomposition process, a Si/MgO mixture formed after a magnesiothermic reduction process, and the final 3D porous Si obtained after an additional two-stage acid etching process.

details. After these pretreatments, according to inductively coupled plasma (ICP) analysis (Fig. 2*B*), the purity of the silica reaches 99.92%, implying that most other residual components were removed completely. It should be noted that although a single step of heat treatment can also generate silica from RHs, the acid treatment is essential in the present study. With a heat treatment alone, the purity of silica reaches only 95.48% (Table S1) because some metal components still remain. The acid treatment should be used to remove these residual metals by the formation of water-soluble metal chlorides. More importantly, the acid treatment is critical in preserving the original porous nanostructure all the way to the final formation of Si, which is very crucial for the stable operation of Si anodes. The same synthetic procedure, but with no acid treatment, would generate Si with the porous nanostructure collapsed (SEM image in Fig. S3). This is attributed to the fact that residual metals (Na, Ca, K, etc.) can generate ternary oxides such as $Na_6Si_8O_{19}$ and $Na_2Si_2O_5$ via reactions with silica (18, 19) and can melt at ~780 °C (20, 21). The use of HCl may not be a critical issue for the scale-up of the given synthetic procedure because HCl treatments have been well adopted in various industrial productions (22, 23). On the other hand, the purity of 95.48% resulting from the heat treatment alone is substantially higher than those of the other silica resources, such as quartz, bentonite, and diatomaceous earth, which are prepared by similar procedures. This shows that rice plants have naturally developed a process for the production of high-purity silica in their RHs. In addition, an X-ray diffraction (XRD) pattern (Fig. 2*C*) of the pretreated RH silica exhibits a broad peak around $2\Theta = 22.5°$, which is characteristic of amorphous silica.

The pretreated RH silica preserves the unique 3D porous structure that originates from the outer epidermis of natural RHs and is also desirable for good performance of the Si anode. Fig. 2 *D* and *E* shows SEM images of the RH silica viewed from the outer surface of an RH at low and high magnifications, respectively. These images clearly confirm that the nanoporous

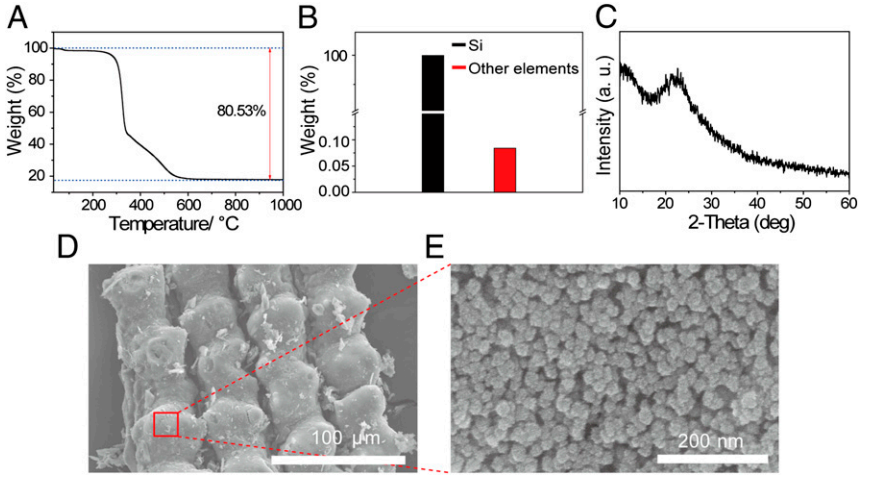


**Fig. 2.** Characterization of pretreated rice husk-originated silica. (*A*) A thermogravimetric analysis (TGA) curve of acid-leached rice husks indicating that the leached rice husks contain 19.5 wt% of silica. (*B*) Elemental analysis of the rice husk-originated silica after the acid-leaching and thermal treatment. Other elements include Al, B, Ba, Ca, Co, Cr, K, La, Li, Mn, Na, Ni, P, S, Ti, V, Zn, Zr, and Mg. (*C*) An XRD pattern of the rice husk-originated silica. (*D*) An SEM image of the rice husk-originated silica viewed from the outer surface. (*E*) The porous nanostructured silica magnified from the red box in *D*.

structure is well maintained in the pretreated RH silica. The porous nature of the pretreated RH silica was supported further by porosity measurements (Fig. S4*A*). Nitrogen adsorption–desorption experiments exhibit an isotherm that corresponds to type IV with a distinct hysteresis loop at high relative pressures ($P/P_0$), indicating that the pretreated RH silica is a mesoporous material. The Barrett–Joyner–Halenda (BJH) pore-size distribution showing a peak at 5 nm also supports the dominant presence of mesopores.

In an effort to transfer the desirable 3D porous structure of the RH silica to Si, a magnesiothermic reduction was carried out at 850 °C for 3 h. After the reduction, the converted Si retains similar bulk-scale morphology to that of the RH silica (Fig. 3*A*). However, the nanoporous structure of the RH silica was changed to an interconnected 3D porous wall structure (Fig. 3*B*), and this change was reflected in the decrease in the specific surface area (SSA) (286 → 47.3 $m^2/g$, Fig. S4 *A* and *B*). In the magnesiothermic reduction process, Si is produced through the following reaction: $SiO_{2(s)} + Mg_{(g)} \rightarrow Si_{(s)} + 2MgO_{(s)}$. In this reaction, solid magnesium (bp = 650 °C) functions as a reducing agent that first evaporates and then diffuses into $SiO_2$. Thus, in our samples, the Mg gas is able to get access to the surfaces deep inside the RH silica through the interconnected nanopores. As a result, a uniformly distributed Si/MgO mixture was produced (Fig. S5 *A*–*E*) without the formation of secondary phases like magnesium silicide ($Mg_2Si$) (Fig. S5*E*), in contrast to reports in the literature (24, 25). Even after selective removal of MgO by acid etching, the interconnected porous structure was observed, but, once again, the structure was changed, to an interconnected porous wall structure, which is attributed to the etching of MgO as well as grain growth during the high-temperature process. See the schematic illustration and corresponding SEM images in Fig. S5*F*.

The morphology and composition of the 3D porous Si were characterized further, using various analytical tools. The scanning transmission electron microscopy (STEM) and high-resolution transmission electron microscopy (HRTEM) images (Fig. 3 *C* and *D*) show clearly that the RH-originated Si has an interconnected porous wall structure with a wall thickness of ~13 nm and a pore diameter of 10~50 nm, which is indeed consistent with the pore size distribution result (Fig. S4*B*). The HRTEM image (Fig. 3*D*, *Lower Inset*) also shows lattice fringes corresponding to the Si (111) lattice, indicating the crystalline character of the 3D porous Si. The crystalline structure was also confirmed by

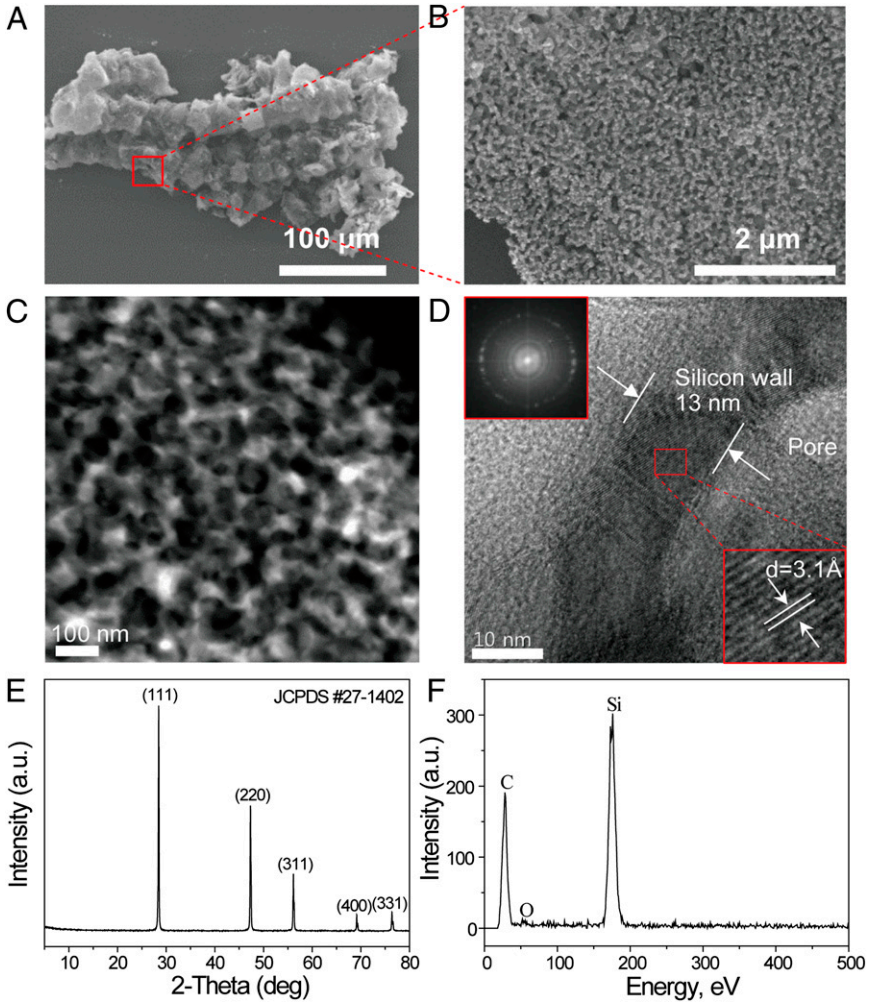


**Fig. 3.** Characterization of rice husk-originated Si. (*A* and *B*) SEM image (*A*) of rice husk-originated Si and its high-magnification image (*B*) magnified from the red box in *A*. (*C*) STEM image of the rice husk-originated Si exhibiting an interconnected 3D porous structure. (*D*) HRTEM image of the 3D porous Si wall structure. The Si wall thickness is ~13 nm. (*Upper Inset*) Selected area electron diffraction (SAED) showing a diffraction ring that corresponds to the (111) lattices of Si. (*Lower Inset*) HRTEM image showing the (111) lattice fringes with a *d*-spacing of 3.1 Å. (*E*) XRD pattern of the rice husk-originated Si with the major lattice orientations denoted. (*F*) Energy-dispersive X-ray spectrum of the rice husk-originated Si (carbon: sample holder line).

selected-area electron diffraction (SAED) (Fig. 3*D*, *Upper Inset*) that exhibits a diffraction ring corresponding to the Si (111) lattice. In addition, the XRD (Fig. 3*E*) and EDS (Fig. 3*F*) spectra verify the pure phase of the crystalline Si, as well as the complete removal of the MgO through the following reaction: $MgO + 2HCl \rightarrow MgCl_2 + H_2O$. From an ICP measurement, the purity of the 3D porous Si was found to be 99.5%, further confirming the formation of pure phase Si.

To evaluate the RH Si as a LIB anode, coin-type half-cells were prepared. See *Materials and Methods* for details. For this testing, we coated the RH Si with carbon layers to compensate for the intrinsically low electronic conductivity of Si as shown in previous studies (26–28). Also, having noted the critical effect of the carbon precursor on the properties of resultant coating layers (26), we chose polydopamine as a precursor material. It has been found that dopamine polymerization yields highly conformal polymer layers with a fine-tuning capability of the coating thickness (26, 28, 29). In the current investigation, after the polydopamine coating and subsequent carbonization, the coating thickness and carbon content were measured to be ∼3–10 nm and 12 wt%, respectively (Fig. S6). The Raman spectroscopy data (Fig. S6*D*) exhibit peaks at 1,360 $cm^{-1}$ (D band, disordered) and 1,589 $cm^{-1}$ (G band, graphene), suggesting an amorphous characteristic of the carbon layers. More importantly, the fine thickness control of the polydopamine layers fulfilled an important function, as the unique porosity of the RH Si was well maintained. Surface area measurements indicated that the carbon-coated Si had an SSA of 87 $m^2/g$ and the pore size distribution with a major pore diameter of ∼10–50 nm was similar to that of the same sample before the carbon coating (Fig. S4*C*). Hereafter, we denote the carbon-coated RH Si as c-$Si_{RH}$.

The electrochemical testing of c-$Si_{RH}$ was conducted primarily by galvanostatic measurements. Detailed measurement conditions are described in *Materials and Methods*. The first cycle shows the characteristic potential profile of crystalline Si (Fig. 4*A*). When measured at 0.1 C (1 C: 2,000 mA/g), lithiation and delithiation took place at 0.1 V and 0.42 V vs. $Li/Li^+$, respectively, and a reversible capacity of 1,615 mAh/g was observed. These values verify, again, the complete reduction of silica and the formation of pure Si. Remarkably, the first coulombic efficiency (CE) of c-$Si_{RH}$ is 84.2%. Such excellent CE suggests that the interconnected porous structure enables the formation of stable SEI layers during the first cycle. Although carbon coating of Si has been known to improve the first CE in general (30), the present case of $Si_{RH}$ exhibits an equally high first CE of 83.9% even before the carbon coating (Fig. S7*A*), implying that the interconnected nanoporous structure of $Si_{RH}$ plays a major role for the high first CE. From control experiments (Fig. S7 *B* and *C*) based on bare carbonized polydopamine and Super P as well as their weight contents (8 and 20 wt%), it turns out that the capacity contributions from both carbonaceous additives are only 1% and 2%, respectively, of the total reversible capacity of c-$Si_{RH}$ (= 1,615 mAh/g). See *SI Text* for detailed calculation.

Moreover, c-$Si_{RH}$ shows excellent discharge capacity retention during cycling using the stable interconnected porous structure. As displayed in Fig. 4*B*, the cycling performance of c-$Si_{RH}$ is clearly better than those of bare Si nanoparticles (NPs) and carbonized polydopamine-coated Si NPs (c-Si NPs). After 50 cycles, c-$Si_{RH}$, c-Si NPs, and Si NPs retain 100%, 36%, and 20% of their initial capacities, respectively. c-Si NPs show improved retention compared with the bare Si NPs, but are still inferior to c-$Si_{RH}$, perhaps because NP-to-NP connection and SEI layers in c-Si NPs still become unstable during cycling. Upon extended cycling, c-$Si_{RH}$ continues to show outstanding capacity retention, as it retains 100% of the original capacity (1,554 mAh/g) after

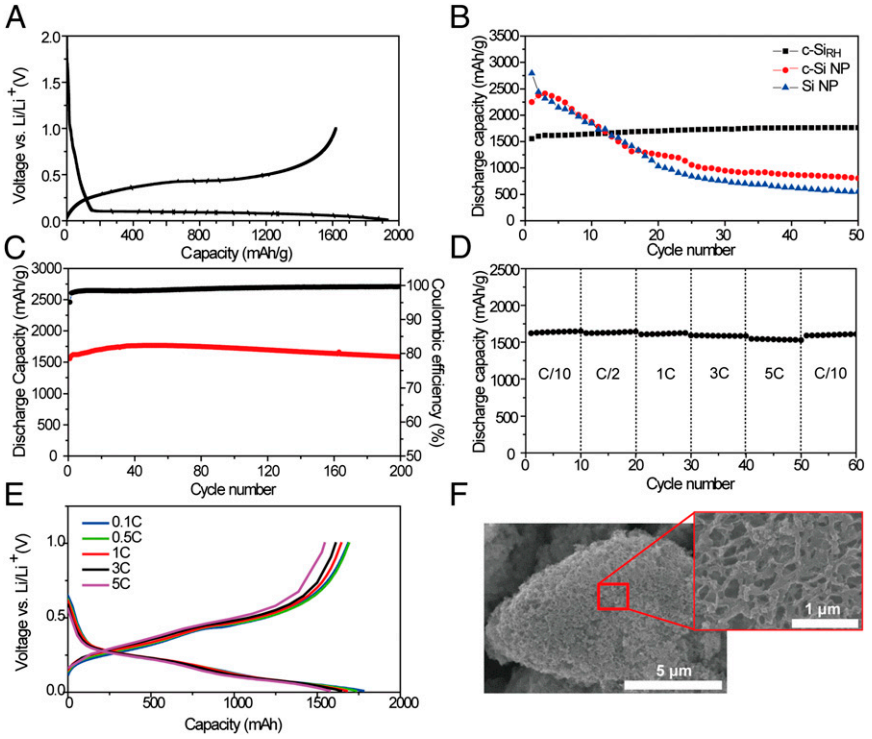


**Fig. 4.** (*A*) Voltage profiles in the first cycle measured at 0.1 C for the carbon-coated rice husk-originated Si (c-$Si_{RH}$) electrode. (*B*) Delithiation capacities of c-$Si_{RH}$, c-Si NPs, and bare Si NPs over cycling. (*C*) Delithiation capacities and CEs of c-$Si_{RH}$, cycled between 0.01 and 1.0 V vs. $Li^+/Li$. In both *B* and *C*, both charge and discharge were measured at a rate of 2 A/g (= 1 C). (*D* and *E*) Delithiation capacities (*D*) and voltage profiles (*E*) of c-$Si_{RH}$ at various discharge rates from 0.1 C to 5 C (1 C = 2 A/g). The charge rate was fixed at 0.1 C. (*F*) SEM images of c-$Si_{RH}$ after 50 cycles.

200 cycles when measured at a rate of 1 C (2,000 mA/g) (Fig. 4*C*). Also, the capacities and CEs during an additional 300 cycles measured at a higher rate of 3 C (6,000 mA/g) are presented in Fig. S8 *A* and *B*. During this cycling period, the capacity retention is 82%, and the average CE is 99.7%. These excellent capacity retentions suggest that the 3D interconnected porous structure originating from outer shells of natural RHs is advantageous and avoids the serious issues of Si anode deterioration, such as particle pulverization (12, 13, 31) and the formation of an unstable SEI (12, 32) that result from the repeated volume change of Si. Although the good capacity retentions of c-$Si_{RH}$ could be attributed partially to the moderate mass loading of Si (~0.3 mg/cm$^2$), the clearly superior performance of c-$Si_{RH}$ compared with that of c-Si NPs verifies the critical role of the interconnected nanoporous structure of $Si_{RH}$ in the cycling performance. The superior cycling performance of c-$Si_{RH}$ becomes more prominent when the mass loading of Si increases significantly by five times to ~1.5 mg/cm$^2$, as c-$Si_{RH}$ retains 72% of the initial capacity after 100 cycles, but c-Si NPs retain only 23% even after 50 cycles (Fig. S8*C*).

Also, c-$Si_{RH}$ shows good rate capability (Fig. 4*D*). To evaluate this, the charge rate was fixed at 0.2 A/g and the discharge rate was varied from 0.2 A/g to 10 A/g. Even when the discharge rate was increased 50 times from 0.1 C to 5 C, c-$Si_{RH}$ retained 95.3% of the original discharge capacity (1,686 mAh/g) (Fig. 4*E*). This excellent rate performance is ascribed to the presence of a uniform carbon coating associated with polydopamine layers, as well as to the small wall thickness of the porous structure that facilitates efficient electronic and ionic diffusion. The SEM image of the c-$Si_{RH}$ electrode taken after 50 cycles exhibits the well-maintained interconnected porous structure, verifying the robust nature of the c-$Si_{RH}$ electrode.

## Conclusions

The present study demonstrates that rice husks, a major by-product in rice harvest, can be used to produce Si with an ideal porous nanostructure for use in high-capacity LIB anodes. Its interconnected nanoporous structure, developed via years of natural evolution for efficient cultivation of rice, can resolve important issues in Si anode operation, enabling excellent cycling and power performance. Given that annual rice production reaches hundreds of millions of tons on a global scale, the promising battery data herein show how a part of the waste from one of the most popular crops, rice husks, can be a resource that helps meet the ever-increasing demand for Si in advanced batteries.

## Materials and Methods

**Fabrication of 3D Nanoporous Si from Rice Husks.** The RHs used in the current study were obtained as a by-product of rice harvested in the suburbs of Daejeon in the Republic of Korea. The RHs were used as raw materials. The RHs were leached with a 10% (wt/vol) HCl solution to remove alkali metal impurities. To remove organic components, a thermal treatment was performed at 650 °C for 3 h. After these two steps, high-quality RH-originated silica was produced. The reduction of the RH-originated silica was conducted by magnesiothermic reduction. For the reduction, 4 g of the pretreated silica and 3.24 g of magnesium were introduced into a silicon carbide crucible and were well mixed. The filled crucible was closed tightly in an argon-filled glove box and was then moved to a furnace. The reduction was carried out at a temperature of 850 °C for 3 h ($2Mg + SiO_2 \rightarrow 2MgO + Si$). After the Mg reduction, high-purity 3D porous silicon was generated by two-stage etching. The collected magnesia/silicon mixture was stirred in 1 M HCl solution (HCl:$H_2O$:EtOH ratio = 0.66:4.72:8.88 in molar ratio) for 5 h at room temperature to selectively remove MgO ($MgO + 2HCl \rightarrow MgCl_2 + H_2O$). The HCl-etched silicon was then treated in HF solution (HF:$H_2O$:EtOH = 1.05:1.11:6.45 in molar ratio) to remove residual silica. For carbon coating of the chemically etched 3D porous Si, the $Si_{RH}$ were first coated with polydopamine, which was subsequently carbonized to form carbon-coating layers. For this step, 0.4 g of $Si_{RH}$ was dispersed in 10 mM Tris buffer solution (pH 8.5, 200 mL) and was sonicated for 20 min. Next, 0.4 g of 2-(3,4-dihydroxyphenyl) ethylamine hydrochloride [dopamine hydrochloride, 98% (vol/vol); Aldrich] was added and stirred for 24 h in the presence of oxygen for polymerization of dopamine. Once the polymerization was completed, $Si_{RH}$ were filtered and rinsed with double-deionized water (DDW) three times to remove residual monomers, which was followed by a drying step under vacuum at 70 °C for 24 h. Finally, the dried polydopamine-coated Si was thermal treated at 800 °C for 3 h for the carbonization.

**Characterization of the Rice Husk-Originated Silica and Si.** The cross-sectional morphologies of RHs were investigated using an optical microscope (Olympus BX-51). XRD [Rigaku; D/MAX-2500 (18 kW)] spectra were acquired using CuKα radiation (λ = 1.5418 Å) to analyze the crystal structures of the RH-originated silica and silicon. The morphologies of the RH-originated silica and silicon were characterized by field emission scanning electron microscopy (FESEM) (HITACHI, S-4800/UHR-SEM; FEI, Magellan 400) and HRTEM (FEI; Tecnai G2 F30). An EDS attached to the SEM and TEM apparatus was used for local elemental analyses. The silica weight portion in the pretreated RHs and the Si weight portion in the carbon-coated 3D porous Si (c-$Si_{RH}$) were obtained on the basis of TGA (NETZSCH; TG 209 F3) measurements. The nitrogen adsorption and desorption isotherms were attained using the Brunauer-Emmett-Teller (BET) (Micrometrics; ASAP2010) method after degassing the samples at 383 K for 5 h. The concentrations of impurities in the RH-originated silica and Si were measured using an ICP-mass spectrometer (PerkinElmer; 5300DV). Raman spectroscopy (excitation, 514 nm) (high-resolution dispersive Raman microscope, Horiba Jobin Yvon; LabRAM HR UV/vis/NIR) was used to investigate the characteristics of carbon-coating layers. To verify the robust structural nature of the electrodes after cycling, the coin cells were opened and the electrodes were thoroughly washed with acetonitrile inside a glove box. Then, the electrodes were transferred to a SEM holder and the holder was completely sealed to prevent exposure to air. The samples were exposed to air for <30 s during the transfer to the vacuum chamber of SEM.

**Battery Testing of 3D Porous Si.** For the electrode fabrication, slurries were prepared by dissolving 60 wt% c-$Si_{RH}$, 20 wt% Super P, and 20 wt% poly (acrylic) acid (PAA) ($M_r$ = 3,000,000; Aldrich) in *N*-methyl-2-pyrrolidone (NMP). The slurries were cast onto a copper current collector (18-μm-thick Cu foil; Hohsen) by using the doctor blade technique. The loading of the active materials was 0.3 mg/cm$^2$. The cast electrodes were dried at 70 °C for 10 h and punched into circular discs for coin-cell fabrication. Lithium hexafluorophosphate ($LiPF_6$) solution (1 M) in a mixture of ethylene carbonate (EC) and diethyl carbonate (DEC) (EC:DEC = 1:1, vol/vol) with 5 wt% fluoroethylene carbonate (PANAX E-TEC) was used as the electrolyte. To test the electrochemical properties, 2,032 type coin cells were assembled in an argon-filled glove box with a dew point below –60 °C at 25 °C. The cells were assembled by sandwiching separators (polypropylene; Celgard 2400) with the Si electrodes (working electrodes) and lithium metal (Honjo; reference/counter electrode). The cells were electrochemically cycled between 0.01 and 1.0 V vs. $Li/Li^+$ at 0.2 A/g under a constant current mode for both charge and discharge in the first cycle and cycled at different current rates thereafter using a cycle tester (PNE Solution).

**ACKNOWLEDGMENTS.** We acknowledge the financial support from a National Research Foundation of Korea (NRF) grants funded by the Korean Ministry of Education and Science Technology (MEST) (NRF-2010-0029031 and NRF-2012-R1A2A1A01011970).

1. Estevez M, Vargas S, Castaño V, Rodriguez R (2009) Silica nano-particles produced by worms through a bio-digestion process of rice husk. *J Non-Cryst Solids* 355(14):844–850.
2. Sun L, Gong K (2001) Silicon-based materials from rice husks and their applications. *Ind Eng Chem Res* 40(25):5861–5877.
3. Ma JF, Yamaji N (2006) Silicon uptake and accumulation in higher plants. *Trends Plant Sci* 11(8):392–397.
4. Tamai K, Ma JF (2003) Characterization of silicon uptake by rice roots. *New Phytol* 158(3):431–436.
5. Epstein E (1994) The anomaly of silicon in plant biology. *Proc Natl Acad Sci USA* 91(1):11–17.
6. Ma JF, et al. (2006) A silicon transporter in rice. *Nature* 440(7084):688–691.
7. Bruce PG, Scrosati B, Tarascon JM (2008) Nanomaterials for rechargeable lithium batteries. *Angew Chem Int Ed Engl* 47(16):2930–2946.
8. Scrosati B, Hassoun J, Sun YK (2011) Lithium-ion batteries. A look into the future. *Energy Environ Sci* 4(9):3287–3295.
9. Zhou W, Upreti S, Whittingham MS (2011) High performance Si/MgO/graphite composite as the anode for lithium-ion batteries. *Electrochem Commun* 13(10):1102–1104.

10. Chen Z, Christensen L, Dahn JR (2003) Large-volume-change electrodes for Li-ion batteries of amorphous alloy particles held by elastomeric tethers. *Electrochem Commun* 5(11):919–923.
11. Key B, et al. (2009) Real-time NMR investigations of structural changes in silicon electrodes for lithium-ion batteries. *J Am Chem Soc* 131(26):9239–9249.
12. Wu H, et al. (2012) Stable cycling of double-walled silicon nanotube battery anodes through solid-electrolyte interphase control. *Nat Nanotechnol* 7(5):310–315.
13. Cho J (2010) Porous Si anode materials for lithium rechargeable batteries. *J Mater Chem* 20(20):4009–4014.
14. Magasinski A, et al. (2010) High-performance lithium-ion anodes using a hierarchical bottom-up approach. *Nat Mater* 9(4):353–358.
15. Yu Y, et al. (2010) Reversible storage of lithium in silver-coated three-dimensional macroporous silicon. *Adv Mater* 22(20):2247–2250.
16. Institute of Information Technology (2011) *LIB Related Study Program 11-12* (Institute of Information Technology, Tokyo).
17. Pijarn N, Jaroenworaluck A, Sunsaneeyametha W, Stevens R (2010) Synthesis and characterization of nanosized-silica gels formed under controlled conditions. *Powder Technol* 203(3):462–468.
18. Allendorf MD, Spear KE (2001) Thermodynamic analysis of silica refractory corrosion in glass-melting furnaces. *J Electrochem Soc* 148(2):B59–B67.
19. Besmann TM, Spear KE (2004) Thermochemical modeling of oxide glasses. *J Am Ceram Soc* 85(12):2887–2894.
20. Hessien M, Rashad M, Zaky R, Abdel-Aal E, El-Barawy K (2009) Controlling the synthesis conditions for silica nanosphere from semi-burned rice straw. *Mater Sci Eng B* 162(1):14–21.
21. Yazhenskikh E, Hack K, Müller M (2006) Critical thermodynamic evaluation of oxide systems relevant to fuel ashes and slags. Part 1: Alkali oxide–silica systems. *Calphad* 30(3):270–276.
22. Dufault R, et al. (2009) Mercury from chlor-alkali plants: Measured concentrations in food product sugar. *Environ Health* 8(1):2.
23. Migahed M, Nassar I (2008) Corrosion inhibition of Tubing steel during acidization of oil and gas wells. *Electrochim Acta* 53(6):2877–2882.
24. Bao Z, et al. (2007) Chemical reduction of three-dimensional silica micro-assemblies into microporous silicon replicas. *Nature* 446(7132):172–175.
25. Chen W, Fan Z, Dhanabalan A, Chen C, Wang C (2011) Mesoporous silicon anodes prepared by magnesiothermic reduction for lithium ion batteries. *J Electrochem Soc* 158(9):A1055–A1059.
26. Liu N, et al. (2012) A yolk-shell design for stabilized and scalable li-ion battery alloy anodes. *Nano Lett* 12(6):3315–3321.
27. Hu YS, et al. (2008) Superior storage performance of a Si@SiOx/C nanocomposite as anode material for lithium-ion batteries. *Angew Chem Int Ed Engl* 47(9): 1645–1649.
28. Liu R, et al. (2011) Dopamine as a carbon source: The controlled synthesis of hollow carbon spheres and yolk-structured carbon nanocomposites. *Angew Chem Int Ed Engl* 50(30):6799–6802.
29. Zhao Y, Liu X, Li H, Zhai T, Zhou H (2012) Hierarchical micro/nano porous silicon Li-ion battery anodes. *Chem Commun* 48(42):5079–5081.
30. Bang BM, Lee JI, Kim H, Cho J, Park S (2012) High-performance macroporous bulk silicon anodes synthesized by template-free chemical etching. *Adv Energy Mater* 2(7): 878–883.
31. Bang BM, Kim H, Song HK, Cho J, Park S (2011) Scalable approach to multi-dimensional bulk Si anodes via metal-assisted chemical etching. *Energy Environ Sci* 4(12):5013–5019.
32. Szczech JR, Jin S (2011) Nanostructured silicon for high capacity lithium battery anodes. *Energy Environ Sci* 4(1):56–72.